Active Wireless Sensing: A Versatile Framework for Information Retrieval in Sensor Networks

Thiagarajan Sivanadyan and Akbar M. Sayeed

***Abstract*—Many existing information processing schemes in sensor networks are based on multi-hop in-network algorithms that require information routing and coordination between nodes and incur excess overhead in latency and energy consumption. In this paper, we develop an alternative and complementary single-hop approach – Active Wireless Sensing (AWS) – in which a Wireless Information Retriever (WIR) queries a select ensemble of nodes to obtain desired information in a rapid and energy-efficient manner. The basic architecture in AWS consists of: i) a WIR, equipped with an antenna array, interrogates the wireless sensors with wideband space-time waveforms, ii) the sensors modulate the acquired waveforms with their (possibly encoded) measured data and generate an ensemble response to the WIR's interrogation signal, and iii) the WIR extracts the sensor data by exploiting the space-time characteristics of the resulting multipath sensing channel. To facilitate analysis, we propose a canonical family of sensing configurations that represent a simple abstraction of spatial correlation in the signal field or the nature of local cooperation in the network. The concept of source-channel matching is introduced in which the spatio-temporal resolution is adapted to the spatial scale of node correlation in the sensing configurations. Signaling strategies and associated receiver structures at the WIR are developed for different source-channel matching configurations. The performance of AWS is analyzed in different configurations both in terms of reliability and capacity of information retrieval.**

I. Introduction

Wireless sensor networks promise an unprecedented ability to monitor the physical environment through spatially distributed devices that can sense the environment in a variety of modalities and communicate with each other in a wireless fashion [1]–[3]. Inference of relevant information about the sensed signal field, such as the sensor data or some summary statistic, is one of the primary applications of sensor networks. *Energy efficiency* in extracting relevant information is one of the primary constraints in the design of sensor networks, since the sensor nodes are typically battery-powered. Another critical but less recognized constraint is *latency* in information retrieval which comes into play for time-sensitive applications such as rapid detection of critical events or objects. In general, the processes of sensing and communication should be jointly optimized for energy efficiency and low latency.

The original vision of a flat, *ad hoc* communication topology for sensor networks has generated a lot of interest in *in-network processing* where either the network as a whole obtains a consistent estimate or consensus of desired information (see, e.g., [4], [5]), or the distributed information is routed to a decision center (see, e.g., [6]). An underlying assumption is that information is diffused through the network in a *multi-hop* fashion to minimize energy consumption. However, in-networking processing, such as consensus algorithms [4], [5], [7], requires networking protocols for multi-hop routing, resulting in an energy overhead that is often ignored. Furthermore, in-network processing algorithms are iterative in nature (see, e.g., [6]), that results in excess delay that may be unacceptable in time-sensitive tasks, such as rapid detection of critical events. For example, it has been shown that for a network with n nodes, consensus algorithms require $\mathcal{O}(n^{3/2}\sqrt{\log(n)})$ iterations to guarantee convergence with high probability [5]. The resulting energy overhead and increased latency are accentuated by the fact that the spatial characteristics of the sensed signal field are *time-varying* in general and, as a result, information routing protocols may have to be updated over time. From a topological perspective, the $\mathcal{O}(\sqrt{n})$ throughput scaling limit in multi-hop networks [8] suggests that a flat network topology is not scalable. Furthermore, engineering large-scale sensor networks with a completely *ad hoc* topology has been very challenging [9]. Thus, there is renewed interest in other network topologies, such as mesh networks, that combine the structure of a cellular topology with the flexibility of an *ad hoc* configuration.

In this paper we develop the concept of Active Wireless Sensing (AWS) that we proposed in [10], [11] as an alternative and complementary single-hop approach to in-network processing. In AWS, a Wireless Information Retriever (WIR) queries a select ensemble of nodes to obtain desired information in a *rapid* and *energy-efficient* manner. AWS has two primary attributes: i) the sensor nodes are "dumb" in that they have limited computational ability but have relatively sophisticated communication front-ends, and ii) the WIR is computationally powerful and is equipped with a multi-antenna array. The basic architecture in AWS, illustrated in Fig. 1, consists of: i) the WIR interrogates a select ensemble of wireless sensors with wideband space-time waveforms,

Manuscript received XXXX; revised XXXX. This work was supported in part by the US NSF under grant #CCF-0431088. The results in this paper were presented in part at the 5th International Conference on Information Processing in Sensor Networks (IPSN '06), Nashville, TN and at the 44th Annual Allerton Conference on Communication, Control and Computing (Allerton '06), Monticello, IL. The associate editor coordinating the review of this manuscript and approving it for publication was Dr. Subhrakanti Dey.

The authors are with the Department of Electrical and Computer Engineering, University of Wisconsin - Madison, Madison, WI 53706-1691 USA (email: thiagars@cae.wisc.edu; akbar@engr.wisc.edu).

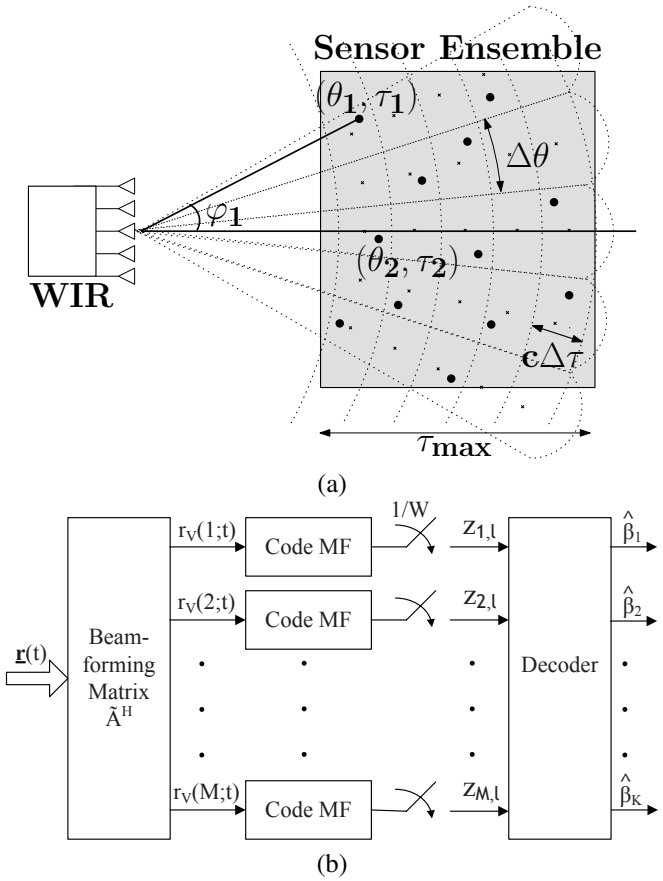

Fig. 1. Active Wireless Sensing. (a) Basic communication architecture. (b) Angle-delay matched filtering at the WIR to compute sufficient statistics.

ii) the sensor modulate their acquired temporal waveforms with (possibly encoded) measurement data, and iii) the WIR extracts sensor data from the ensemble response by exploiting the differences in the space-time characteristics of individual sensor responses. Thus, the computational burden is shifted to the WIR which can also "program" the sensors for different tasks, such as field estimation or event detection.

In contrast to in-network processing, AWS has a definitive advantage in terms of latency.[1] For example, in contrast to the $\mathcal{O}(n^{3/2})$ channel uses required by iterative consensus algorithms [5], AWS can achieve consensus in $\mathcal{O}(1)$ channel uses. In terms of energy efficiency, while the single-hop communication architecture in AWS requires higher energy consumption (due to larger path loss) compared to multi-hop communication for a *single channel use*, the large number of channel uses (or iterations, typically *super-linear* in the number of nodes) required for convergence in in-network algorithms tips the balance in favor of AWS which requires $\mathcal{O}(n)$ transmissions in each channel use. AWS may also serve as a basic building block for scalable mesh networks in which strategically placed WIRs can serve as access points for facilitating network communication, monitoring and control.

Technological advances in agile radio frequency (RF) front-ends and reconfigurable antenna arrays provide another motivation for AWS. WIRs equipped with agile RF transceivers could interrogate the sensor network at varying spatio-temporal resolutions, thereby enabling rapid learning of the spatio-temporal characteristics of the sensor field [12]. Thus, the AWS architecture exploits the advanced functionality afforded by wideband RF front-ends in single-hop architectures in sensor and communication networks where the nodes directly communicate with an access point; see, e.g., [13]–[17]. This ability of AWS also complements ongoing research in *cognitive radio* and *waveform diversity* for agile communication and sensing [18]–[20].

AWS is similar, in terms of the underlying physics, to the concept of Imaging Sensor Nets that has been independently proposed recently [21], [22]. However, the focus of these works, inspired by radar imaging principles, is on sensor localization and detection of spatially well-separated events. The emphasis of AWS, on the other hand, is on sensor information retrieval and the basic concept is inspired by an intimate connection with communication over multiple antenna (MIMO) wireless channels in a multipath environment: sensor nodes act as active scatterers and generate a multipath signal in response to the WIR's interrogation signal. A key idea behind AWS is to separate multiple sensor responses by resolving them in angle and delay at a resolution commensurate with the spatio-temporal signal space, as illustrated in Fig. 1. This is facilitated by a virtual representation of wideband space-time wireless channels that we have developed in the past several years [23]–[26]. The virtual representation yields a natural partitioning of sensor responses in angle-delay and provides a mathematical framework for studying fundamental performance limits of AWS at different spatio-temporal resolutions afforded by agile RF front ends. We believe that Imaging Sensor Nets and AWS provide complementary perspectives on information extraction in sensor networks and could be fruitfully cross-leveraged by exploiting the connections between wideband radar imaging, wireless communications, and waveform diversity techniques.

The goal of this paper is to develop the basic ideas in AWS and we focus on line-of-sight communication between the sensor ensemble and the WIR. Sec. II develops the basic communication architecture in AWS, illustrated in Fig. 1. Sec. III presents canonical sensing configurations that form the basis of the development in this paper and represent a simple abstraction of spatial correlation in the sensed signal field or the nature of local cooperation between nodes. The sensor ensemble is partitioned into spatial coherence regions (SCRs), where the sensors in distinct SCRs transmit independent information whereas the sensors within each SCR send identical information (see also [14]). Sec. IV describes the signal processing at the WIR for different sensing configurations for information retrieval at the *highest spatio-temporal resolution* – each angle-delay matched filter (MF) output in Fig. 1(b) is associated with a *distinct* angle-delay resolution bin in Fig. 1(a) which, in turn, is occupied by a *distinct* sensor. The probability of error in different configurations is analyzed for *uncoded* sensor transmissions. Secs. V and VI discuss the receiver structures and analyze the probability of error for *source-channel matching* (SCM) – the angle-delay resolution is adapted to match the size of each SCR. Each

[1] A comparison of AWS and in-network processing in terms of energy and latency is presented in Sec. VIII.

angle-delay MF output is now associated with a distinct SCR, rather than a distinct sensor, and consists of the superposition of all sensor transmissions within the SCR. Sec. V discusses *incoherent SCM* when the different sensors in each SCR can have different relative phases, whereas Sec. VI discusses *coherent SCM* when the sensors in each SCR transmit in a phase-coherent fashion. Sec. VII discusses *sensing capacity of AWS* – the highest rate of information retrieval attainable through *coded* sensor transmissions – for different sensing configurations. As our results indicate, coherent SCM provides a powerful mechanism for dramatically increasing the energy-efficiency and/or capacity of AWS. In all sections, we present numerical results to illustrate the theory. Sec. VIII compares energy and latency requirements in in-network processing and AWS to achieve consensus. Sec. IX provides concluding remarks and avenues for future research.

II. The Basic Space-Time Communication Architecture

We first outline the basic assumptions made in this work. Consider an ensemble of K sensors uniformly distributed over a region of interest that is interrogated by a wireless information retriever (WIR), as illustrated in Fig. 1(a). We assume that the WIR, equipped with an M-element antenna array, is sufficiently far from the sensor ensemble, in the same plane, so that far-field assumptions apply. Furthermore, there exists a strong line of sight path between the WIR and each sensor (no multipath), and the differences in path loss between individual sensors and the WIR can be neglected due to the large distance between the WIR and the sensor field. The WIR interrogates the sensor ensemble by transmitting wideband (spread spectrum) signaling waveforms, $\{s_m(t)\}$, from different antennas where each $s_m(t)$ is of duration T and (two-sided) bandwidth W. Let $TW \gg 1$ denote the time-bandwidth product of the signaling waveforms that represents the approximate dimension of the temporal signal space. Thus, the signal space of spatio-temporal interrogation waveforms has dimension MTW, and affords a spatial (angular) resolution of $\Delta\theta = 1/M$ and a delay resolution of $\Delta\tau = 1/W$ to distinguish different sensor signals.

We make the practically feasible assumption that the WIR and the sensor nodes are carrier (frequency) synchronized but not phase synchronized. We assume that the relative phase offset between each sensor and the WIR stays constant over at least two channel uses (roughly over a duration of $2T$, as elaborated later), so that phase estimation is possible. Frequency synchronization as well as estimation of the relative sensor phases can be done periodically depending on the sensor oscillator characteristics. As elaborated later, information retrieval at the highest angle-delay resolution, in which distinct sensors are associated with distinct angle-delay resolution bins, constrains the bandwidth to [10]: $c/\Delta d < W < 2f_c/M$ where f_c is the carrier frequency, c is the speed of wave propagation, and Δd is the minimum distance between the sensors in the direction of the WIR. The lower bound guarantees resolution of individual sensors in delay ($\Delta\tau = 1/W < \Delta d/c$), whereas the upper bound guarantees that the relative time delay between the WIR antennas from any given sensor is negligible compared to the delay resolution at critical antenna spacing ($\Delta\tau = 1/W > (M\lambda/2)/c = M/2f_c$). The above constraints imply that $f_c > cM/2\Delta d$. For example, for a sensor separation of $\Delta d = 1$m, a WIR with $M = 10$ antennas uses a signaling bandwidth $W > c/\Delta d = 300$MHz, and a carrier frequency $f_c > cM/2\Delta d = 1.5$GHz.

A. Overview of the Communication Protocol

We now present an overview of the communication protocol in AWS, illustrated in Fig. 2:

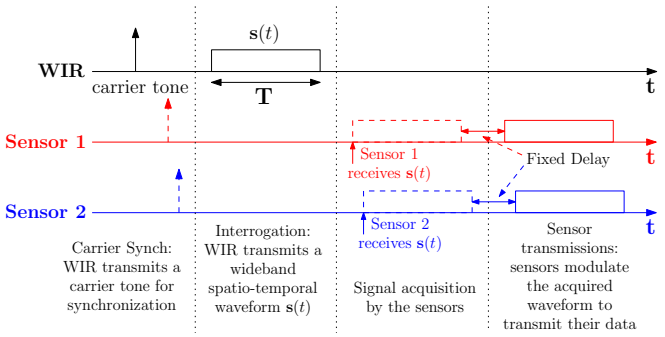

Fig. 2. AWS Communication Protocol

- **Frequency synchronization.** The WIR initiates the process by transmitting a carrier signal to synchronize the frequency of sensors' oscillators.
- **WIR interrogation signal.** The WIR transmits a high power spread-spectrum space-time interrogation waveform to a select ensemble of sensors. For simplicity, we assume that the entire ensemble is queried in the interrogation phase.
- **Sensor waveform acquisition and transmission.** The set of sensors which have data to send are termed "active." In this paper, we assume that all interrogated sensors are active, which is the most challenging scenario. The active sensors encode their data and modulate it onto their temporal signal acquired during the interrogation phase. The sensors transmit their modulated waveforms after a fixed duration (common to all sensors) relative to the timing reference provided by WIR's interrogation waveform. Thus, sensor signals arrive at the WIR at different relative delays that depend on their relative distances to the WIR.
- **Sensor information extraction at the WIR.** The aggregate signal from the active sensors is processed at the WIR to extract the information of interest, such as the individual sensor data or a collective decision statistic.

After the initial interrogation by the WIR, the sensors can continue sending their data using their acquired waveforms. One *channel use* corresponds to the time taken for sensor transmissions ($T_c = T + \tau_{max}$) where $\tau_{max} < T$ is the maximum relative delay between sensor transmissions.

B. The Multipath Sensing Channel in AWS

For simplicity, we consider a one-dimensional uniform linear array (ULA) of antennas and assume M to be odd without

loss of generality (WLOG), and define $\tilde{M} = (M-1)/2$. The normalized array response vector for a ULA is given by

$$\boldsymbol{a}(\theta) = \sqrt{\frac{1}{M}}\left[e^{j2\pi\tilde{M}\theta}, \cdots, 1, \cdots, e^{-j2\pi\tilde{M}\theta}\right]^T \quad (1)$$

where the normalized angle θ is related to the physical angle of arrival/departure φ (see Fig. 1(a)) as $\theta = d\sin(\varphi)/\lambda$. Here d denotes the spacing between the antennas and λ is the wavelength of propagation. Due to the relatively large distance from the WIR, we assume that the sensor ensemble projects a limited angular spread at the WIR array: $\varphi \in [-\varphi_{max}, \varphi_{max}] \subset [-\pi/2, \pi/2]$ and the antenna spacing is chosen larger than the critical $\lambda/2$ spacing[2], $d = \lambda/2\sin(\varphi_{max})$, resulting in a one-to-one mapping between $\theta \in [-0.5, 0.5]$ and $\varphi \in [-\varphi_{max}, \varphi_{max}]$.

The WIR transmits the space-time signal $\boldsymbol{s}(t) = [s_1(t), s_2(t), \ldots, s_M(t)]^T$ in an interrogation packet to initiate information retrieval from the sensor ensemble. The i-th sensor acquires a waveform, $x_i(t)$, given by $x_i(t) = e^{-j\phi_i}\boldsymbol{a}^T(\theta_i)\boldsymbol{s}(t-\tau_i)$, where θ_i denotes the direction of the i-th sensor relative to the WIR array (see Fig. 1(a)), τ_i denotes the relative delay between the i-th sensor and the WIR, and $\phi_i \in [0, 2\pi]$ denotes a (random) relative phase between the WIR and the i-th sensor. We ignore noise in the acquired waveform $x_i(t)$ since the interrogation signal can be sufficiently strong. The i-th sensor encodes its measurement in β_i, modulates $x_i(t)$ by β_i, and transmits it with energy $\mathcal{E}$ after a fixed duration following the reception of the interrogation packet. We assume instantaneous retransmission from each sensor for simplicity of exposition. Thus, the transmitted signal from the i-th sensor can be expressed as $y_i(t) = \beta_i\sqrt{\mathcal{E}}x_i(t) = \beta_i\sqrt{\mathcal{E}}e^{-j\phi_i}\boldsymbol{a}^T(\theta_i)\boldsymbol{s}(t-\tau_i)$, where $E[|\beta_i|^2] = 1$ and we assume waveform normalization at each sensor, $\int |x_i(t)|^2 dt = 1$, so that $y_i(t)$ has energy $\mathcal{E}$. The received vector signal at the WIR, $\boldsymbol{r}(t) = [r_1(t), r_2(t), \cdots, r_M(t)]^T$, is a superposition of all sensor transmissions and it can be expressed as

$$\boldsymbol{r}(t) = \sqrt{\mathcal{E}M}\sum_{i=1}^{K}\beta_i e^{-j\phi_i}\boldsymbol{a}(\theta_i)\boldsymbol{a}^T(\theta_i)\boldsymbol{s}(t-\tilde{\tau}_i) + \boldsymbol{w}(t) \quad (2)$$

where $\sqrt{M}$ reflects the array gain, $\tilde{\tau}_i = 2\tau_i$ denotes the round-trip relative delay in the response from the i^{th} sensor, $\boldsymbol{w}(t)$ denotes a complex vector AWGN (additive white Gaussian noise) process representing the independent noise at different WIR antennas. Assume that $\min_i \tilde{\tau}_i = 0$ and let $\tau_{max} = \max_i \tilde{\tau}_i$ reflect the delay spread in sensor transmissions. Using (2), the effective system equation relating the WIR's received vector signal to the transmitted signal can be expressed as

$$\boldsymbol{r}(t) = \sqrt{\mathcal{E}}\int_0^{\tau_{max}} \boldsymbol{H}(t')\boldsymbol{s}(t-t')dt' + \boldsymbol{w}(t) \quad (3)$$

$$\boldsymbol{H}(t) = \sqrt{M}\sum_{i=1}^{K}\alpha_i\delta(t-\tilde{\tau}_i)\boldsymbol{a}(\theta_i)\boldsymbol{a}^T(\theta_i)\ ,\ \alpha_i = \beta_i e^{-j\phi_i} \quad (4)$$

where the $M\times M$ matrix $\boldsymbol{H}(t)$ represents the impulse response for the *space-time multipath sensing channel* underlying AWS.

[2]We ignore the passive reflections, due to grating lobes, from objects outside the angular spread of the sensor ensemble since the active sensor transmissions will be stronger.

C. Sensor Localization in Angle and Delay

The channel matrix (4) in AWS, relating the transmitted and received signals at the WIR, has exactly the same form as the impulse response of a physical multiple-antenna (MIMO) multipath wireless channel where different sensors act as *active scatterers* and the sensor data and phases $\{\alpha_i = \beta_i e^{-j\phi_i}\}$ correspond to the complex path gains associated with scattering paths in a MIMO multipath channel [23], [24]. In contrast to a MIMO channel, the transmitter and the receiver are co-located (WIR) in AWS. To gain insight into the communication aspects of AWS, we leverage the *virtual representation* of MIMO multipath channels that is a linear, *unitarily equivalent* representation of the physical sensing channel matrix [23], [24]. The virtual representation samples the physical multipath in angle and delay at resolutions $\Delta\theta = 1/M$ and $\Delta\tau = 1/W$ afforded by the spatio-temporal signal space. A key property of the virtual representation is that its coefficients represent a partitioning or resolution of sensors in angle and delay.

The virtual representation in angle corresponds to representing $\boldsymbol{H}(t)$ with respect to beams in M fixed virtual directions: $\tilde{\theta}_m = m\Delta\theta = m/M$, $m = -\tilde{M}, \cdots, \tilde{M}$. Define the $M \times M$ unitary (DFT) matrix, $\boldsymbol{A} = [\boldsymbol{a}(-\tilde{M}/M), \ldots, \boldsymbol{1}, \ldots, \boldsymbol{a}(\tilde{M}/M)]$, whose columns are the normalized steering vectors for the virtual angles and form an orthonormal basis for the spatial signal space. The virtual spatial matrix $\boldsymbol{H}_v(t)$ is unitarily equivalent to $\boldsymbol{H}(t)$ as

$$\boldsymbol{H}(t) = \boldsymbol{A}\boldsymbol{H}_v(t)\boldsymbol{A}^T \leftrightarrow \boldsymbol{H}_v(t) = \boldsymbol{A}^H\boldsymbol{H}(t)\boldsymbol{A}^* \quad (5)$$

and the virtual channel coefficients, the elements of $\boldsymbol{H}_v(t)$, representing the coupling between the m-th transmit beam and m'-th receive beam at the WIR are given by

$$H_v(m', m; t) = \boldsymbol{a}^H(m'/M)\boldsymbol{H}(t)\boldsymbol{a}^*(m/M) \quad (6)$$

$$\approx H_v(m, m; t)\delta_{m-m'} \quad (7)$$

$$H_v(m, m; t) \approx \sqrt{M}\left[\sum_{i\in S_{\theta,m}}\alpha_i g^2\left(\theta_i - \frac{m}{M}\right)\right]\delta(t-\tilde{\tau}_i) \quad (8)$$

where $g(\theta) = \boldsymbol{a}^H(\theta)\boldsymbol{a}(0) = \frac{1}{M}\frac{\sin(\pi M\theta)}{\sin(\pi\theta)}$, $g(0) = 1$, is the Dirichlet sinc function that captures the interaction between the fixed virtual beam directions and the physical sensor directions, δ_m denotes the kronecker delta function, and the approximation in (7) is due to the fact that $g(\theta)$ is peaky at the origin and $g(\theta_i - m/M)g(\theta_i - m'/M) \approx \delta_{m-m'}$ [23].[3] The approximation in (8) follows from *path partitioning* induced by the virtual representation [23]:

$$S_{\theta,m} = \left\{i \in \{1, \cdots, K\} : -\frac{\Delta\theta}{2} < \theta_i - m\Delta\theta \leq \frac{\Delta\theta}{2}\right\} \quad (9)$$

denotes the set of all sensors whose angles lie in the m-th spatial resolution bin of width $\Delta\theta = 1/M$, centered around the m-th beam (see Fig. 1(a)). Thus, virtual representation in angle partitions the sensors in angle: $\boldsymbol{H}_v(t)$ is approximately diagonal and its m-th diagonal entry contains the superposition of all sensor responses that lie within the m-th beam.

[3]The approximation gets more accurate with increasing M.

The sensor responses within each spatial beam can be further partitioned by resolving their delays with resolution $\Delta\tau = 1/W$. Let $L = \lceil \tau_{max} W \rceil$ denote the normalized delay spread. The diagonal entries of virtual spatial matrix in (7) can be decomposed into virtual, uniformly spaced delays as [24]

$$H_v(m,m;t) \approx \sum_{\ell=0}^{L-1} H_v(m,m,\ell)\delta(t-\ell/W) \quad (10)$$

$$h_v(m,\ell) = H_v(m,m,\ell) \quad (11)$$

$$= \sqrt{M}\sum_{i=1}^{K} \alpha_i g^2\left(\theta_i - \frac{m}{M}\right)\mathrm{sinc}(W\tilde{\tau}_i - \ell)$$

$$\approx \sqrt{M}\sum_{i\in S_{\theta,m}\cap S_{\tau,\ell}} \alpha_i g^2\left(\theta_i - \frac{m}{M}\right)\mathrm{sinc}(W\tilde{\tau}_i - \ell) \quad (12)$$

where $\mathrm{sinc}(x) = \sin(\pi x)/\pi x$, $\mathrm{sinc}(0) = 1$, captures the interaction between the virtual and physical sensor delays, and

$$S_{\tau,\ell} = \left\{ i \in \{1,\cdots,K\} : -\frac{\Delta\tau}{2} < \tilde{\tau}_i - \ell\Delta\tau \le \frac{\Delta\tau}{2} \right\} \quad (13)$$

is the set of all sensors whose delays lie within the ℓ-th delay resolution bin of width $\Delta\tau = 1/W$ (see Fig. 1(a)). As illustrated in Fig. 1(a), the virtual coefficient $h_v(m,\ell) = H_v(m,m,\ell)$ in (12), associated with the (m,ℓ)-th angle-delay resolution bin, is a superposition of all sensor responses whose angles and delays lie in the intersection of the m-th spatial beam and ℓ-th delay ring.

Summarizing the above development, the virtual angle-delay representation of $\boldsymbol{H}(t)$ in (4) is given by

$$\boldsymbol{H}(t) = \boldsymbol{A}\boldsymbol{H}_v(t)\boldsymbol{A}^T \approx \boldsymbol{A}\left[\sum_{\ell=0}^{L-1}\boldsymbol{H}_v[\ell]\delta\left(t-\frac{\ell}{W}\right)\right]\boldsymbol{A}^T \quad (14)$$

$$= \sum_{\ell=0}^{L-1}\sum_{m=-\tilde{M}}^{\tilde{M}} h_v(m,\ell)\boldsymbol{a}\Big(\frac{m}{M}\Big)\boldsymbol{a}^T\Big(\frac{m}{M}\Big)\delta\Big(t-\frac{\ell}{W}\Big) \quad (15)$$

and the corresponding $\boldsymbol{r}(t)$ in (3) is given by

$$\boldsymbol{r}(t) \approx \sqrt{\mathcal{E}}\sum_{\ell=0}^{L-1}\boldsymbol{A}\boldsymbol{H}_v[\ell]\boldsymbol{A}^T\boldsymbol{s}(t-\ell/W) + \boldsymbol{w}(t) \quad (16)$$

$$= \sqrt{\mathcal{E}}\sum_{m,\ell} h_v(m,\ell)\boldsymbol{a}\left(\frac{m}{M}\right)\boldsymbol{a}^T\left(\frac{m}{M}\right)\boldsymbol{s}\left(t-\frac{\ell}{W}\right) + \boldsymbol{w}(t) \quad (17)$$

where $\boldsymbol{H}_v[\ell]$ is the $M \times M$ (approximately) diagonal virtual spatial matrix corresponding to the ℓ-th resolvable delay with diagonal entries given by $\{h_v(m,\ell) : m = -\tilde{M},\cdots,\tilde{M}\}$ defined in (12). The above virtual representation of the sensing channel matrix $\boldsymbol{H}(t)$ is exploited in the next section to develop the receiver structure at the WIR for extracting sensor information from $\boldsymbol{r}(t)$.

D. Angle-Delay Sufficient Statistics at Highest Resolution

We now describe the basic processing of the received signal $\boldsymbol{r}(t)$ at the WIR for computing the sufficient statistics for information retrieval, as illustrated in Fig. 1(b). Define $\boldsymbol{s}(t) = \boldsymbol{A}^*\boldsymbol{s}_v(t)$ and $\boldsymbol{r}_v(t) = \boldsymbol{A}^H\boldsymbol{r}(t)$, where $\boldsymbol{s}_v(t) = [s_v(-\tilde{M};t),\cdots,s_v(\tilde{M};t)]^T$ and $\boldsymbol{r}_v(t) = [r_v(-\tilde{M};t),\cdots,r_v(\tilde{M};t)]^T$ denote the M-dimensional transmitted and received signals in the virtual spatial domain (beamspace). In our model, $\boldsymbol{s}_v(t)$ represents the temporal spread-spectrum waveforms transmitted by the WIR and acquired by the sensors in different virtual spatial beam directions. We assume that each $s_v(m;t)$ is a *unit-energy* pseudo-random spread-spectrum waveform with bandwidth W and duration T (e.g., a direct-sequence spread spectrum waveform [27]) and, thus, we have[4]

$$\langle s_v(m;t-\ell/W), s_v(m;t-\ell'/W)\rangle \approx \delta_{\ell-\ell'} \ . \quad (18)$$

Using (16), the equation that relates the transmitted and received signals at the WIR in beamspace is

$$\boldsymbol{r}_v(t) = \boldsymbol{A}^H\boldsymbol{r}(t) = \sqrt{\mathcal{E}}\sum_{\ell=0}^{L-1}\boldsymbol{H}_v[\ell]\boldsymbol{s}_v(t-\ell/W) + \boldsymbol{w}_v(t) \quad (19)$$

where $\boldsymbol{w}_v(t) = \boldsymbol{A}^H\boldsymbol{w}(t)$ represents a vector of independent temporal AWGN processes with power spectral density σ^2. Note that since $\boldsymbol{H}_v[\ell]$ is (approximately) diagonal, the relation in (19) is equivalent to M scalar equations, each relating $r_v(m;t)$ to $s_v(m;t)$. Thus, using the orthogonality property in (18), correlating each $r_v(m;t)$ with delay versions of $s_v(m;t)$ yields the sufficient statistics for information retrieval at the WIR for one sensor packet transmission

$$z_{m,\ell} = \langle r_v(m;t), s_v(m;t-\ell/W)\rangle \quad (20)$$

$$= \int_0^{T+\tau_{max}} r_v(m;t)s_v^*(m;t-\ell/W)dt \quad (21)$$

$$= \sqrt{\mathcal{E}}h_v(m,\ell) + w_{m,\ell} \quad (22)$$

where $m = -\tilde{M},\cdots,\tilde{M}, \ell = 0,\cdots,L-1$ and $\{w_{m,\ell}\}$ are i.i.d. complex Gaussian with variance σ^2.

While different temporal waveforms can be assigned to different spatial beams in AWS, as discussed above, in the rest of the paper we focus on the attractive special case in which the same unit-energy spread-spectrum waveform, $c(t)$, is transmitted in all spatial beams; that is, $s_v(m;t) = c(t)$ for all m or $\boldsymbol{s}_v(t) = \mathbf{1}c(t)$ where $\mathbf{1}$ denotes a vector of ones. In this case, all sensors acquire the same waveform $c(t)$ and the transmitted signal from the i-th sensor takes the form $y_i(t) = \sqrt{\mathcal{E}}\beta_i e^{-j\phi_i}c(t-\tau_i)$ and the composite received signal at the WIR is given by

$$\boldsymbol{r}(t) = \sqrt{M\mathcal{E}}\sum_{i=1}^{K}\beta_i e^{-j\phi_i}\boldsymbol{a}(\theta_i)c(t-\tilde{\tau}_i) + \boldsymbol{w}(t) \quad (23)$$

$$\approx \sum_{\ell=0}^{L-1}\sum_{m=-\tilde{M}}^{\tilde{M}} h_v(m,\ell)\boldsymbol{a}\left(\frac{m}{M}\right)c\left(t-\frac{\ell}{W}\right) + \boldsymbol{w}(t) \quad (24)$$

The corresponding angle-delay MF outputs in (21) for one

[4]The cross-correlation is on the order of $1/N = 1/TW$ and thus very small for large N.

information packet are given by

$$z_{m,\ell} = \int_0^{T+\tau_{max}} \boldsymbol{a}^H(m/M)\boldsymbol{r}(t)c^*(t-\ell/W)dt \quad (25)$$

$$= \sqrt{M\mathcal{E}}\sum_{i=1}^{K}\beta_i\gamma_i(m,\ell) + w_{m,\ell} \quad (26)$$

$$\approx \sqrt{\mathcal{E}}h_v(m,\ell) + w_{m,\ell} \quad (27)$$

$$\gamma_i(m,\ell) = e^{-j\phi_i}g\left(\theta_i - \frac{m}{M}\right)\mathrm{sinc}(W\tau_i - \ell) \quad (28)$$

where $\gamma_i(m,\ell)$ represents the contribution of the i-th sensor, based on its location, to the (m,ℓ)-th MF output. Stacking the MF outputs in a $ML \geq K$ dimensional vector, we have

$$\boldsymbol{z} = \sqrt{M\mathcal{E}}\boldsymbol{\Gamma}\boldsymbol{\beta} + \boldsymbol{w} = \sqrt{M\mathcal{E}}\sum_{i=1}^{K}\beta_i\boldsymbol{\gamma}_i + \boldsymbol{w} \quad (29)$$

where $\boldsymbol{\Gamma} = [\boldsymbol{\gamma}_1, \boldsymbol{\gamma}_2, \cdots, \boldsymbol{\gamma}_K]$ is the $ML \times K$ coupling matrix that maps the sensor data vector, $\boldsymbol{\beta} = [\beta_1 \ldots \beta_K]^T$, to the angle-delay MF output vector $\boldsymbol{z} = \{z_{m,\ell}\}$, and $\sqrt{M}$ reflects the array gain. The column vector $\boldsymbol{\gamma}_i = \{\gamma_i(m,\ell)\}$ represents the *angle-delay signature* generated by the i-th sensor.

As discussed earlier, the sensor responses in the second equality in (27) are partitioned into different $h_v(m,\ell)$'s in the third approximation based on the virtual representation:

$$h_v(m,\ell) \approx \sqrt{M}\sum_{i\in S_{\theta,m}\cap S_{\tau,\ell}}\beta_i\gamma_i(m,\ell)\ . \quad (30)$$

However, in order to separate sensor responses, we require that distinct sensors correspond to distinct angle-delay MF outputs. For a given number of antennas M and a given minimum spacing between sensors Δd in the direction of the WIR, the bandwidth W can be chosen sufficiently large, in principle, so that there is exactly one sensor in each angle-delay resolution bin: $|S_{\theta,m}\cap S_{\tau,\ell}| = 1$. Specifically, we require $c\Delta\tau = c/W < \Delta d \leftrightarrow W > c/\Delta d$. In this **highest-resolution** sensing case, we can define one-to-one mappings $i(m,\ell)$ and $(m(i),\ell(i))$ that associate each sensor with a *unique* angle-delay resolution bin. It follows that the (m,ℓ)-th MF output in (27) primarily contains the data transmitted by the $i(m,\ell)$-th sensor: $h_v(m,\ell) \approx \sqrt{M}\beta_{i(m,\ell)}\gamma_{i(m,\ell)}(m,\ell)$. Conversely, the signature, $\gamma_i(m,\ell)$, in (28) of the i-th sensor has one dominant entry, $\gamma_i(m(i),\ell(i))$, corresponding to the angle-delay bin associated with the i-th sensor. As a result, each angle-delay signature is approximately unit-norm, $\|\boldsymbol{\gamma}_i\|^2 = \sum_{m,\ell}|\gamma_i(m,\ell)|^2 \approx |\gamma_i(m(i),\ell(i))|^2 \approx 1$. We refer to the $K \leq ML$ angle-delay resolution bins occupied by distinct transmitting sensors to be active. All further development in this paper assumes that $K = ML$ (also see Rem. 2).

Remark 1 (Ideal Case): When the sensors positions coincide with the center of the resolution bins; that is, $(\theta_i,\tau_i) = (m(i)/M, \ell(i)/W)$ for some $m(i) \in \{-\tilde{M},\ldots,\tilde{M}\}$ and $\ell(i) \in \{0,\ldots,L-1\}$, $\gamma_i(m,\ell) = e^{-j\phi_i}\delta_{m-m(i)}\delta_{\ell-\ell(i)}$. Consequently, $\gamma_i(m,\ell)$ has a single non-zero value corresponding to $(m(i),\ell(i))$-th angle-delay bin. It follows that the different sensor angle-delay signatures are orthonormal, $\boldsymbol{\gamma}_i^H\boldsymbol{\gamma}_k = \delta_{i-k}$, and with appropriate re-ordering of sensors, $\boldsymbol{\Gamma}$ is diagonal (as illustrated in Fig. 3(a)): $\boldsymbol{\Gamma} = \boldsymbol{\Phi} = \mathrm{diag}(e^{-j\phi_1},\cdots,e^{-j\phi_K})$ and $\boldsymbol{\Gamma}^H\boldsymbol{\Gamma} = \boldsymbol{I}$. As a result, the (m,ℓ)-th MF output contains only the data transmitted from the corresponding sensor: $z_{m,\ell} = \sqrt{M\mathcal{E}}\beta_{i(m,\ell)}e^{-j\phi_{i(m,\ell)}} + w_{m,\ell}$. □

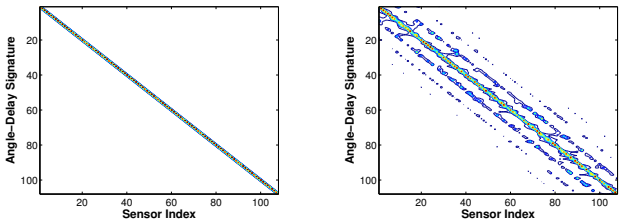

(a) (b)

Fig. 3. Signature matrix $\boldsymbol{\Gamma}$ contour plots. (a) Ideal case. (b) Non-ideal case.

In general, when the sensor locations do not coincide with the center of angle-delay bins, $\boldsymbol{\gamma}_i(m,\ell)$ has multiple non-zero components with the largest one in the $(m(i),\ell(i))$-th angle-delay bin and smaller values in other bins. As a result, $\boldsymbol{\Gamma}$ has off-diagonal terms, as illustrated in Fig. 3(b), and there is interference between sensor transmissions. We will address the issue of interference suppression later.

Remark 2 (Phase Estimation Errors): All the P_e expressions in this paper assume coherent signaling with perfect knowledge of the sensor phases $\{\phi_i\}$ at the WIR. In practice, an initial training packet of known symbols may be transmitted from all the active sensors which allows the WIR to first determine the location of active bins/sensors by thresholding the MF outputs, and then reliably estimate the corresponding phases [10]. Alternately, we can use non-coherent (on-off) signaling with energy detection at the WIR [10], which incurs a 3dB SNR loss compared to the coherent case. A complete analysis of the impact of phase estimation errors is beyond the scope of this paper. □

Remark 3 (Distributed MIMO Interpretation): Thus far we have emphasized the roundtrip channel relating the transmitted and received signals at the WIR. The rest of the paper is focussed on the channel coupling the sensor ensemble to the WIR as described by (29). This represents a semi-distributed MIMO channel coupling the K distributed sensor transmissions $\boldsymbol{\beta}$ and the $K = ML$ angle-delay MF outputs $\boldsymbol{z}$ at the WIR. The channel is characterized by the signature matrix $\boldsymbol{\Gamma}$ that is diagonally dominant in general and exactly diagonal in the ideal case (see Fig. 3).

III. Canonical Sensing Configurations

We now present a family of canonical sensing configurations in AWS that form the basis of the development in this paper. To start with, we consider uncoded BPSK transmissions from sensors: $\{\beta_i \in \{-1,+1\}\}$. In Sec. VII we discuss the sensing capacity which may be attained with coded transmissions.

In the canonical sensing configurations, illustrated in Fig. 4, the $K = ML$ active sensors are partitioned into K_{ind} groups or *spatial coherence regions (SCRs)*, each group consisting of K_{coh} sensors so that $K = K_{ind}K_{coh}$. We assume that all the K_{coh} sensors in each group transmit the same bit, whereas the bits from distinct groups are independent. That is, $\beta_i = \tilde{\beta}_\mu$ for all $i \in S_\mu$, where S_μ is the group of sensors

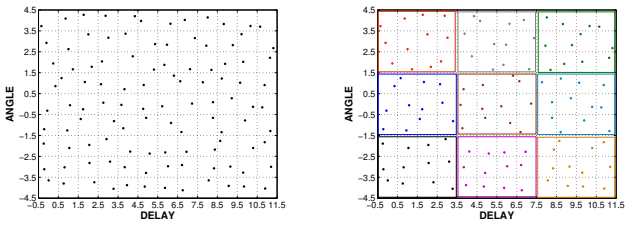

(a) (b)

Fig. 4. Canonical sensing configurations at maximum resolution for $K = ML = 9 \times 12 = 108$ active sensors. The sensors are partitioned as $K = K_{ind}K_{coh}$ into K_{ind} groups (SCRs) with K_{coh} sensors in each SCR. (a) Independent transmissions from all sensors ($K_{ind} = K = 108$). (b) $K_{ind} = 9$ SCRs with $K_{coh} = 12$ sensors transmitting each independent bit.

in the μ-th SCR and the different $\tilde{\beta}_\mu$, $\mu = 1, \ldots, K_{ind}$, are independent. Thus, K_{ind} bits of information are retrieved in each channel use. With the above partitioning, and an appropriate re-ordering of sensors, the K-dimensional sensor data vector $\boldsymbol{\beta} = [\beta_1, \ldots, \beta_K]^T$ in (29) can be expressed as

$$\boldsymbol{\beta} = \boldsymbol{U}\tilde{\boldsymbol{\beta}} = \begin{bmatrix} \mathbf{1}_{K_{coh}} & \mathbf{0} & \cdots & \mathbf{0} \\ \mathbf{0} & \mathbf{1}_{K_{coh}} & \cdots & \mathbf{0} \\ \vdots & \vdots & \ddots & \mathbf{0} \\ \mathbf{0} & \mathbf{0} & \cdots & \mathbf{1}_{K_{coh}} \end{bmatrix} \begin{bmatrix} \tilde{\beta}_1 \\ \tilde{\beta}_2 \\ \vdots \\ \tilde{\beta}_{K_{ind}} \end{bmatrix} \tag{31}$$

where $\mathbf{1}_{K_{coh}}$ is a column vector of length K_{coh} containing all ones representing the identical transmissions from the sensors in an SCR. The matrix $\boldsymbol{U}$ is a $K \times K_{ind}$ matrix that maps the K_{ind}-dimensional vector, $\tilde{\boldsymbol{\beta}}$, of independent bits to the K-dimensional, $\boldsymbol{\beta}$, of sensor transmissions.

The above sensing configurations are an idealized abstraction of correlated sensor measurements: all sensors within each SCR have highly correlated measurements, whereas the sensor measurements in different groups are statistically independent. This may reflect the intrinsic correlations in the sensor measurements of a homogeneous signal field [14], or may reflect the result of in-network processing where sensors within a group arrive at a consensus statistic reflected in their common bit. The higher the value of K_{coh}, the higher the sensor correlation and thus fewer $K_{ind} = K/K_{coh}$ bits capture the information in the sensor ensemble. We note that arbitrary sensing configurations, with non-uniform and non-rectangular SCRs can also be used. From a distributed MIMO perspective (Rem. 3), K_{ind} reflects the *multiplexing gain* – the number of independent parallel (interfering) channels between the sensor ensemble and the WIR – and K_{coh} reflects the number of sensors contributing to each parallel channel.

The next section discusses receiver processing at the WIR for information retrieval at the *highest resolution* for different canonical configurations (values of K_{ind}). Sec. V discusses the case of *incoherent source-channel matching* in which the angle-delay resolution is matched to the size of the SCRs. Sec. VI discusses the case of *coherent source-channel matching* in which the sensors in each SCR transmit in a coherent fashion. In each section, we develop the receiver structures for estimating the independent bits, $\tilde{\boldsymbol{\beta}}$, at the WIR and derive expressions for the associated probability of error.

IV. Information Retrieval at Highest Resolution

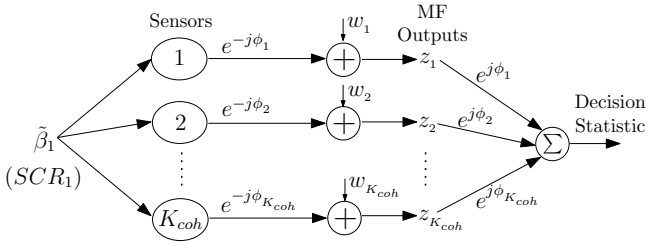

Fig. 5. Information retrieval at the highest resolution. K_{coh} parallel channels created between the sensors in each SCR and the WIR.

In this section, we describe the signal processing at the WIR for information retrieval in the canonical sensing configurations at the highest resolution: each angle-delay bin corresponds to a distinct sensor. We consider two receiver structures – with or without interference suppression – and analyze the resulting probability of error, P_e, in retrieving the K_{ind} bits of information in each channel use.

Analogous to the sensor re-ordering in (31), we assume WLOG that the first K_{coh} MF outputs correspond to the first group, S_1, the second K_{coh} outputs to S_2 and so on. With this re-ordering and (31), the MF output vector can be written as

$$\boldsymbol{z} = [\boldsymbol{z}_1^T, \boldsymbol{z}_2^T, \cdots, \boldsymbol{z}_{K_{ind}}^T]^T = \sqrt{M\mathcal{E}}\boldsymbol{\Gamma}\boldsymbol{U}\tilde{\boldsymbol{\beta}} + \boldsymbol{w} \tag{32}$$

$$= \sqrt{M\mathcal{E}}\boldsymbol{Q}\tilde{\boldsymbol{\beta}} + \boldsymbol{w} = \sqrt{M\mathcal{E}}\sum_{i=1}^{K_{ind}} \tilde{\beta}_i \boldsymbol{q}_i + \boldsymbol{w} \tag{33}$$

where the $K_{coh} \times 1$ vector $\boldsymbol{z}_i$ corresponds to the sensors in the i-th SCR and

$$\boldsymbol{Q} = \boldsymbol{\Gamma}\boldsymbol{U} = [\boldsymbol{q}_1, \boldsymbol{q}_2, \cdots, \boldsymbol{q}_{K_{ind}}] \ , \ \boldsymbol{q}_i = \sum\nolimits_{k \in S_i} \boldsymbol{\gamma}_k \ . \tag{34}$$

The $K \times K_{ind}$ matrix $\boldsymbol{Q}$ is the *effective signature matrix* that couples the K_{ind} independent bits in $\tilde{\boldsymbol{\beta}}$ to the K MF outputs $\boldsymbol{z}$, and $\boldsymbol{q}_i$ is the *effective angle-delay signature* associated with the bit $\tilde{\beta}_i$ from the i-th SCR. Note that $\|\boldsymbol{q}_i\|^2 \approx K_{coh}\|\boldsymbol{\gamma}_i\|^2 = K_{coh}$ reflects the contribution of K_{coh} sensors to each bit.

Remark 4 (Ideal Case): Since $\boldsymbol{\Gamma} = \boldsymbol{\Phi}$ is diagonal (see Rem. 1), (34) implies that $\boldsymbol{q}_i$ has K_{coh} non-zero values of unit magnitude in the angle-delay bins corresponding to the sensors in the i-th SCR, that contribute to the corresponding MF outputs, $\boldsymbol{z}_i$, as illustrated in Fig. 5. Thus, the different $\boldsymbol{q}_i$ are orthogonal, $\boldsymbol{q}_i^H\boldsymbol{q}_k = \sum_{j_1 \in S_i}\sum_{j_2 \in S_k} \boldsymbol{\gamma}_{j_1}{}^H\boldsymbol{\gamma}_{j_2} = K_{coh}\delta_{i-k}$, $\boldsymbol{Q}^H\boldsymbol{Q} = \boldsymbol{U}^H\boldsymbol{\Phi}^H\boldsymbol{\Phi}\boldsymbol{U} = K_{coh}\boldsymbol{I}$, and $\|\boldsymbol{q}_i\|^2 = K_{coh}$. □

A. Angle-Delay Signature Matched Filtering

In general, the angle-delay signatures, $\{\boldsymbol{q}_i\}$, are not orthogonal. Due to interference between them, it is well-known that the optimum maximum likelihood (ML) detector of the independent bit vector $\tilde{\boldsymbol{\beta}}$

$$\hat{\tilde{\boldsymbol{\beta}}} = \arg \max_{\tilde{\boldsymbol{\beta}} \in \{-1,1\}^{K_{ind}}} \|\boldsymbol{z} - \sqrt{M\mathcal{E}}\boldsymbol{Q}\tilde{\boldsymbol{\beta}}\|^2 \tag{35}$$

has exponential complexity in K_{ind} (see, e.g., [28]). The simplest receiver simply ignores the interference and match

filters to the effective angle-delay signatures corresponding to the different SCRs

$$\hat{\tilde{\boldsymbol{\beta}}}_{mf} = \text{sign}\{\text{Re}(\boldsymbol{Q}^H \boldsymbol{z})\} \tag{36}$$

The i-th component of the decision statistic, $\tilde{\boldsymbol{z}} = \boldsymbol{Q}^H \boldsymbol{z}$, can be expressed as

$$\tilde{z}_i = \sqrt{M\mathcal{E}}(\boldsymbol{q}_i{}^H \boldsymbol{q}_i)\tilde{\beta}_i + \sqrt{M\mathcal{E}} \sum\nolimits_{k \neq i} (\boldsymbol{q}_i{}^H \boldsymbol{q}_k)\tilde{\beta}_k + \boldsymbol{q}_i{}^H \boldsymbol{w} \ . \tag{37}$$

Using the Gaussian approximation for the interference (second term in (37)), the P_e for the i-th bit can be characterized as [28] $P_{e,mf}(i) = Q(\sqrt{2\text{SINR}_{mf}(i)})$ where the Signal-to-Interference-and-Noise-Ratio (SINR) is given by

$$\text{SINR}_{mf}(i) = \frac{M\mathcal{E}\|\boldsymbol{q}_i\|^4}{M\mathcal{E}\sum_{k\neq i}|\boldsymbol{q}_i^H \boldsymbol{q}_k|^2 + \|\boldsymbol{q}_i\|^2\sigma^2} \ . \tag{38}$$

Define the per-sensor transmit SNR as $\rho_{sen} = \frac{\mathcal{E}}{\sigma^2}$. In general, the MF detector is interference-limited since the P_e exhibits an error floor in the limit of high ρ_{sen}

$$P_{e,mf}(i) \to Q\left(\sqrt{\frac{2\|\boldsymbol{q}_i\|^4}{\sum_{k\neq i}|\boldsymbol{q}_i{}^H \boldsymbol{q}_k|^2}}\right) \text{ as } \rho_{sen} \to \infty. \tag{39}$$

Under ideal conditions, the interference term in (38) vanishes, and the P_e reduces to

$$P_{e,mf,ideal} = Q\left(\sqrt{2\text{SNR}}\right) = Q\left(\sqrt{\frac{2M\mathcal{E}\|\boldsymbol{q}_i\|^2}{\sigma^2}}\right) \tag{40}$$

$$= Q\left(\sqrt{\frac{2M\mathcal{E}}{\sigma^2}\left(\frac{K}{K_{ind}}\right)}\right) = Q\left(\sqrt{\frac{2M\mathcal{E}K_{coh}}{\sigma^2}}\right) \tag{41}$$

which is the P_e for BPSK signaling over an AWGN channel with K_{coh} times the individual sensor power. The M-fold increase in the received SNR at the WIR is due to array gain. The above formula reveals a basic *rate-versus-reliability tradeoff* in AWS at the highest resolution: *increase in rate by increasing K_{ind} (multiplexing gain) comes at the cost of loss in reliability (SNR) due to a decrease in K_{coh}.*

B. Linear MMSE Interference Suppression

As noted above, the P_e based on angle-delay signature matched filtering suffers from an error floor. Interference is particularly acute for higher values of K_{ind}. Thus, methods for mitigating interference are critical for energy-efficient operation in AWS. The communication channel from the sensor ensemble to the WIR is a multiple access channel (MAC) and the different sensors are analogous to multiple users simultaneously accessing the channel with distinct angle-delay signatures. Thus, a range of multiuser detection techniques can be leveraged [28]. In particular, low-complexity linear interference suppression techniques can yield competitive performance [28]. We consider a simple linear minimum-mean-squared-error (MMSE) interference suppression technique [28], [29]. The MMSE detector takes the form

$$\begin{aligned} \hat{\tilde{\boldsymbol{\beta}}}_{mmse} &= \text{sign}\left\{\text{Re}\left(\boldsymbol{L}_{mmse}\boldsymbol{z}\right)\right\} &(42)\\ \boldsymbol{L}_{mmse} &= \arg\min_{\boldsymbol{L}} E[\|\boldsymbol{L}\boldsymbol{z} - \tilde{\boldsymbol{\beta}}\|^2] = \boldsymbol{Q}^H \boldsymbol{R}^{-1} \ . &(43)\end{aligned}$$

The $K_{ind} \times K$ matrix $\boldsymbol{L}_{mmse}$ denotes the MMSE filter and $\boldsymbol{R} = E[\boldsymbol{z}\boldsymbol{z}^H] = M\mathcal{E}\boldsymbol{Q}\boldsymbol{Q}^H + \sigma^2\boldsymbol{I}$ is the correlation matrix of the MF outputs. In (43), $\boldsymbol{R}^{-1}$ suppresses the interference corrupting the MF outputs and the matrix $\boldsymbol{Q}^H$ performs angle-delay signature matched filtering on the resulting filtered MF outputs. The i-th filtered decision statistic in $\tilde{\boldsymbol{z}} = \boldsymbol{L}_{mmse}\boldsymbol{z}$, $\tilde{z}_i$, $i = 1, \ldots, K_{ind}$, can be expressed as

$$\begin{aligned}\tilde{z}_i =& \sqrt{M\mathcal{E}}\boldsymbol{q}_i{}^H \boldsymbol{R}^{-1}\boldsymbol{q}_i\tilde{\beta}_i \\ &+ \sqrt{M\mathcal{E}}\sum\nolimits_{k\neq i} \boldsymbol{q}_i{}^H \boldsymbol{R}^{-1}\boldsymbol{q}_k\tilde{\beta}_k + \boldsymbol{q}_i{}^H \boldsymbol{R}^{-1}\boldsymbol{w}\end{aligned} \tag{44}$$

where $\boldsymbol{q}_i{}^H \boldsymbol{R}^{-1}\boldsymbol{q}_i$ represents the filtered desired signal and $\boldsymbol{q}_i{}^H \boldsymbol{R}^{-1}\boldsymbol{q}_k$ the suppressed interference from the k-th SCR. Using a Gaussian approximation for the interference [28], the P_e can be expressed as

$$\begin{aligned} P_{e,mmse}(i) &= Q\left(\sqrt{2\text{SINR}_{mmse}(i)}\right) \\ &= Q\left(\sqrt{\frac{2M\mathcal{E}|\boldsymbol{q}_i{}^H \boldsymbol{R}^{-1}\boldsymbol{q}_i|^2}{\sigma^2\|\boldsymbol{q}_i{}^H \boldsymbol{R}^{-1}\|^2 + M\mathcal{E}\sum\limits_{k\neq i}|\boldsymbol{q}_i{}^H \boldsymbol{R}^{-1}\boldsymbol{q}_k|^2}}\right)\end{aligned} \tag{45}$$

In the high SNR regime, the SINR can alternately be expressed in terms of the eigen decomposition of the interference as [30]: $\text{SINR}_{mmse}(i) \approx M\mathcal{E}\|\boldsymbol{q}_{\perp,i}\|^2/\sigma^2$ where $\boldsymbol{q}_{\perp,i} = \boldsymbol{U}_{\perp,i}\boldsymbol{U}_{\perp,i}^H\boldsymbol{q}_i$. The matrix $\boldsymbol{U}_{\perp,i}$ contains the eigenvectors corresponding to the zero eigenvalues in the eigen decomposition of the interference covariance matrix, $\boldsymbol{R}_{int,i}$, where

$$\boldsymbol{R} = M\mathcal{E}\boldsymbol{q}_i\boldsymbol{q}_i^H + M\mathcal{E}\boldsymbol{R}_{int,i} + \sigma^2\boldsymbol{I} \ \text{ and } \ \boldsymbol{R}_{int,i} = \sum_{k\neq i}\boldsymbol{q}_k\boldsymbol{q}_k^H \ . \tag{46}$$

If $ML \geq K$ and the matrix $\boldsymbol{Q}$ is full rank, then $\boldsymbol{q}_{\perp,i}$, the component of $\boldsymbol{q}_i$ that lies perpendicular to the interference (and therefore interference free), is always non-zero and the SINR does not saturate. Hence, the P_e associated with MMSE filtering does not suffer from error floors [28] as confirmed by the numerical results presented in the next section.

C. Numerical Results

We now illustrate the performance of information retrieval at the highest resolution with numerical results. We consider a WIR equipped with $M = 9$ antennas which transmits a single spread-spectrum waveform in all virtual spatial beams: $s_V(m;t) = c(t)$ for all m, where a length $TW = 127$ pseudo-random binary code is used for $c(t)$. We assume that the transmission delays from the sensors to the WIR fall within $L = 12$ delay bins, resulting in a total of $ML = 108$ angle-delay resolution bins at the highest resolution.

The P_e as a function of the per-sensor transmit SNR, ρ_{sen}, is shown in Fig. 6(a) for different values of K_{ind}. The ideal P_e curves correspond to the ideal case with no interference. All other P_e (non-ideal) curves correspond to the average performance over multiple random positions of the sensors within their respective bins, and the P_e reflects the average performance across all active sensors. As K_{ind} decreases, the required SNR for a given P_e is reduced due to an increase

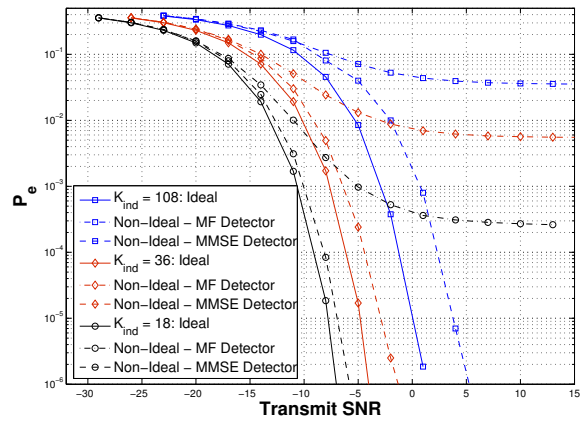

(a)

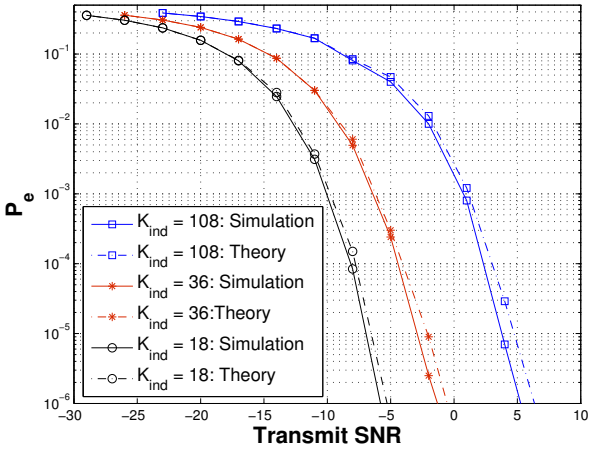

(b)

Fig. 6. (a) P_e vs SNR plots for an AWS system retrieving K_{ind} bits per channel use at maximum angle-delay resolution. (b) Comparison of the analytically computed P_e with numerically estimated values.

in K_{coh}. Furthermore, the MF detector incurs a loss in SNR compared to the ideal case and also exhibits a P_e floor due to interference; with increasing K_{ind}, the interference level increases and the P_e saturates at a larger value. On the other hand, the MMSE detector delivers remarkable performance and exhibits no error floors. Fig. 6(b) compares the numerically estimated values of P_e (for the MMSE detector in Fig. 6(a)) with the corresponding analytic expression in (45) based on the Gaussian approximation. As evident, the agreement is quite good.

V. Incoherent Source-Channel Matching

In information retrieval at the highest resolution, each angle-delay resolution bin is associated with a distinct sensor. In effect, K parallel (interfering) channels are created between the K sensors and the WIR via angle-delay matched filtering. However, in the canonical sensing configurations, the K_{coh} sensors in each SCR transmit the same bit and thus do not need to be individually resolved. In this section, we consider the case of incoherent source-channel matching (ISCM) in

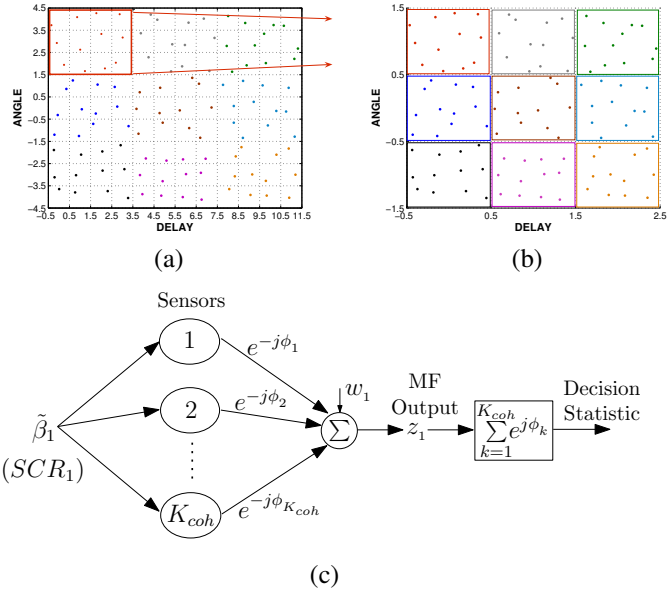

Fig. 7. Illustration of incoherent source-channel matching (ISCM). (a) Active bins at the WIR at the highest resolution corresponding to a canonical sensing configuration with $K_{ind} = 12$ and $K = 108$. (b) $K_{ind} = 12$ active angle-delay resolution bins at the WIR corresponding to ISCM via reduced angle-delay resolution; K_{coh} sensors incoherently contribute to each angle-delay bin. (c) The K_{coh} sensor transmissions in each SCR are mapped to a single MF output, in effect creating a $K_{coh} \times 1$ incoherent MAC between each SCR and the WIR.

which the angle-delay resolution is matched to the size of the SCR's. As illustrated in Fig. 7(a) and (b), in ISCM the angle-delay resolution is reduced so that each angle-delay bin corresponds to a distinct SCR rather than a distinct sensor as in the high-resolution case. In effect, the K_{coh} parallel channels between each SCR and the WIR at the highest resolution are transformed into an *incoherent* $K_{coh} \times 1$ MAC, since the sensor phases in each SCR can be different. Thus, there are K_{ind} distinct angle-delay resolution bins at the WIR (as opposed to K bins at the highest resolution) and the K_{coh} sensor transmissions from each SCR incoherently contribute to the corresponding angle-delay bin, as illustrated in Fig. 7(c) (compare with Fig. 5).

The idea of reduced angle-delay resolution to realize ISCM is illustrated in Fig. 7 for $K = 108$, $K_{ind} = 9$ and $K_{coh} = 12$. Let $K_{ind} = M_{ind}L_{ind} \leftrightarrow K_{coh} = M_{coh}L_{coh}$ so that each SCR with $K_{coh} = 12$ sensors corresponds to $L_{coh} = 4$ delay bins and $M_{coh} = 3$ angle bins at the maximum resolution, as illustrated in Fig. 7(a). ISCM involves two key effects in each SCR, as illustrated in Fig. 7(b): i) the angular resolution is reduced by a factor M_{coh} so that the M_{coh} angle bins in Fig. 7(a) get mapped to a single bin in Fig. 7(b); ii) the delay resolution is reduced by a factor of L_{coh} so that the sensor transmissions in distinct L_{coh} delay bins at the highest resolution in Fig. 7(a) are mapped to a single delay bin in Fig. 7(b). Techniques to realize both these effects in practice are discussed in Sec. VI-B. Alternatively, ISCM may also arise when the sensors are densely spaced compared to the angle-delay resolution so that multiple sensor transmissions contribute to each angle-delay bin.

The effective system equation for ISCM can be inferred

from (33) as

$$\boldsymbol{z}_{isc} = \sqrt{M\mathcal{E}}\boldsymbol{U}^H\boldsymbol{\Gamma}\boldsymbol{U}\tilde{\boldsymbol{\beta}} + \boldsymbol{w}_{isc} = \sqrt{M\mathcal{E}}\sum_{i=1}^{K_{ind}}\tilde{\beta}_i\boldsymbol{d}_i + \boldsymbol{w}_{isc} \tag{47}$$

where $\boldsymbol{z}_{isc} = [z_{isc,1}, z_{isc,2}, \ldots, z_{isc,K_{ind}}]^T$ the $K_{ind} \times K_{ind}$ signature matrix $\boldsymbol{D} = [\boldsymbol{d}_1, \cdots, \boldsymbol{d}_{K_{ind}}]$,

$$\boldsymbol{D} = \boldsymbol{U}^H\boldsymbol{\Gamma}\boldsymbol{U} = \boldsymbol{U}^H\boldsymbol{Q} = [\boldsymbol{U}^H\boldsymbol{q}_1, \cdots, \boldsymbol{U}^H\boldsymbol{q}_{K_{ind}}] \tag{48}$$

represents the coupling between the K_{ind} independent sensor transmissions and the K_{ind} active angle-delay resolution bins at the WIR, and the $K_{ind}\times 1$ vectors, $\boldsymbol{d}_i$, represent the effective angle-delay signatures associated with the i-th transmitted bit $\tilde{\beta}_i$ from the i-th SCR.

The receivers for ISCM can be designed using the system equation (47), parallel to the high-resolution case. The MF detector is given by $\hat{\tilde{\boldsymbol{\beta}}}_{mf} = \text{sign}\left\{\text{Re}\left(\boldsymbol{D}^H\boldsymbol{z}_{isc}\right)\right\}$ and the $P_{e,isc,mf}(i) = Q(\sqrt{2\text{SINR}_{mf}(i)})$ associated with the i-th bit can be estimated using the expression for $\text{SINR}_{mf}(i)$ in (38) by replacing $\{\boldsymbol{q}_i\}$ with $\{\boldsymbol{d}_i\}$. Similarly, the MMSE detector is given by $\hat{\tilde{\boldsymbol{\beta}}}_{mmse} = \text{sign}\left\{\text{Re}\left(\boldsymbol{L}_{isc,mmse}\boldsymbol{z}_{isc}\right)\right\}$ where the $K_{ind} \times K_{ind}$ filter matrix $\boldsymbol{L}_{isc,mmse}$ is given by

$$\boldsymbol{L}_{isc,mmse} = \arg\min_{\boldsymbol{L}} E[\|\boldsymbol{L}\boldsymbol{z}_{isc} - \tilde{\boldsymbol{\beta}}\|^2] = \boldsymbol{D}^H\boldsymbol{R}_{isc}^{-1} \tag{49}$$

and $\boldsymbol{R}_{isc} = E[\boldsymbol{z}_{isc}\boldsymbol{z}_{isc}^H] = M\mathcal{E}\boldsymbol{D}\boldsymbol{D}^H + \sigma^2\boldsymbol{I}$ is the correlation matrix of the MF outputs. The P_e of the MMSE receiver, $P_{e,isc,mmse}(i)$ can be approximated similar to (45) as

$$P_{\substack{e,isc,\\mmse}}(i) = Q\left(\sqrt{\frac{2M\mathcal{E}|\boldsymbol{d}_i{}^H\boldsymbol{R}_{isc}^{-1}\boldsymbol{d}_i|^2}{\sigma^2\|\boldsymbol{d}_i{}^H\boldsymbol{R}_{isc}^{-1}\|^2 + M\mathcal{E}\sum\limits_{k\neq i}|\boldsymbol{d}_i{}^H\boldsymbol{R}_{isc}^{-1}\boldsymbol{d}_k|^2}}\right) \tag{50}$$

The performance of ISCM is dictated by two competing phenomena. On the one hand, reducing the number of MF outputs to match K_{ind} reduces the noise contribution to each MF output. On the other hand, since K_{coh} incoherent sensor transmissions contribute to each MF output, the resulting signal may be weaker or stronger depending on the instantaneous phases. As elaborated next for the ideal case, this effectively results in a fading channel connecting each SCR to the WIR. In particular, the above expressions for P_e are conditioned on a given realization of the sensor phases in each SCR and hence on a particular realization of the signature vectors $\{\boldsymbol{d}_i\}$.

Remark 5 (Ideal Case): When all the sensors in each SCR coincide with the center of the resolution bins at the highest resolution, $\boldsymbol{\Gamma} = \boldsymbol{\Phi}$ is diagonal (see Rem. 1), and from (48) we have $\boldsymbol{D} = \boldsymbol{U}^H\boldsymbol{Q} = \boldsymbol{U}^H\boldsymbol{\Phi}\boldsymbol{U}$. The $K \times 1$ high-resolution signature $\boldsymbol{q}_i$ consists of K_{coh} phase terms in the coordinates corresponding to the i-th SCR (see Rem. 4). Hence, the $K_{ind} \times 1$ signature $\boldsymbol{d}_i = \boldsymbol{U}^H\boldsymbol{q}_i$ in ISCM consists of all zeros except a single non-zero entry which is the sum of K_{coh} independent phases in the coordinate corresponding to the i-th SCR, that is $d_i(n) = \sum_{k\in S_i} e^{-j\phi_k}\delta_{n-i}$. The magnitude of this entry depends on the instantaneous phases of the K_{coh} sensor transmissions in the SCR and as a result $\|\boldsymbol{d}_i\|^2$ is a random quantity with $E[\|\boldsymbol{d}_i\|^2] = K_{coh}$. However, $\boldsymbol{D}$ is diagonal and the different signatures are still orthogonal: $\boldsymbol{D}^H\boldsymbol{D} = \text{diag}(\|\boldsymbol{d}_1\|^2, \cdots, \|\boldsymbol{d}_{K_{ind}}\|^2)$.□

The P_e and SNR expressions in the ideal case are useful to infer the effect of phase incoherence in each SCR in ISCM relative to information retrieval at the highest resolution. The i-th MF output is

$$z_i = \sqrt{M\mathcal{E}}\tilde{\beta}_i\sum\nolimits_{k\in S_i} e^{-j\phi_k} + w_i \tag{51}$$

and the $\sum_{k\in S_i} e^{-j\phi_k}$ term effectively introduces fading (as values of $\{\phi_k\}$ vary) that results in fluctuations in the instantaneous received SNR at the WIR. The average received SNR

$$\text{E}[\text{SNR}(i)] = M\mathcal{E}\text{E}\left[\left|\sum\nolimits_{k\in S_i} e^{-j\phi_i}\right|^2\right]\Big/\,\sigma^2 = M\mathcal{E}K_{coh}/\sigma^2 \tag{52}$$

is the same as that in the highest resolution case. However, since the instantaneous SNR can fluctuate above and below the average, the long-term average probability of error, including averaging over the sensor phases, is given by: $P_{e,isc,ideal} = \text{E}\left[Q\left(\sqrt{2\text{SNR}(i)}\right)\right]$. Modeling $|\sum_{k\in S_i} e^{-j\phi_i}|$ as a Rayleigh random variable (if K_{coh} is sufficiently large), the probability of error can be approximated as [27]

$$\begin{aligned} P_{e,isc,ideal} &\approx \frac{1}{2}\left(1 - \sqrt{\frac{\text{E}[\text{SNR}(i)]}{1+\text{E}[\text{SNR}(i)]}}\right) \\ &\approx \frac{1}{4\text{E}[\text{SNR}(i)]} = \frac{1}{4\rho_{sen}MK_{coh}} \end{aligned} \tag{53}$$

where $\rho_{sen} = \mathcal{E}/\sigma^2$ is the per-sensor transmit SNR. Thus, the performance in ISCM suffers considerably due to the phase incoherence in the sensors' transmissions in each SCR, as illustrated by the numerical results in the next section. Note that the same averaging over sensor phases should be done in earlier expressions for P_e in the general case to compute the long-term average P_e.

A. Numerical Results

We present numerical results to illustrate the performance of AWS in an ISCM configuration. The simulation set up is identical to the one in Sec. IV-C. The probability of error P_e as a function $\rho_{sen} = \mathcal{E}/\sigma^2$ is shown in Fig. 8(a), along with the corresponding plots for the high-resolution case. The P_e for the MMSE detector in ISCM is computed by averaging the expression in (50) over multiple independent phases for the sensors. The scaling behavior of P_e with ρ_{sen} due to fading (see (53) for the ideal case) and the resulting loss in SNR compared to the high-resolution case is evident. Fig. 8(b) compares the numerically estimated values of P_e (for the MMSE detector) with the corresponding averaged value (over phase realizations) of the analytic expression in (50).

VI. Coherent Source-Channel Matching

In maximum resolution sensing, each sensor transmission is associated with a distinct angle-delay bin or MF output, whereas in the canonical sensing configurations, only $K_{ind} \leq K$ independent bits are transmitted and $K_{coh} = K/K_{ind}$ sensors in each group transmit the same bit (see Fig. 5). These

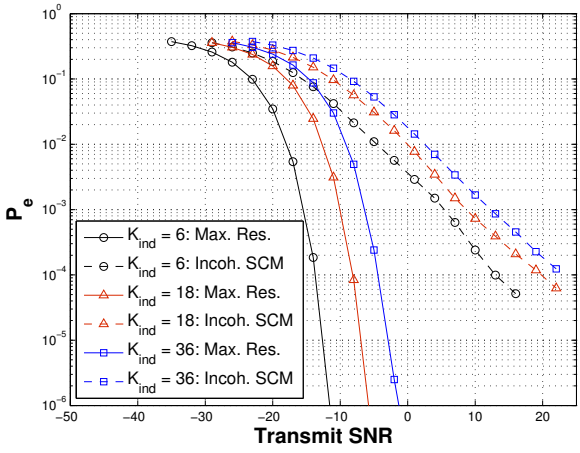

(a)

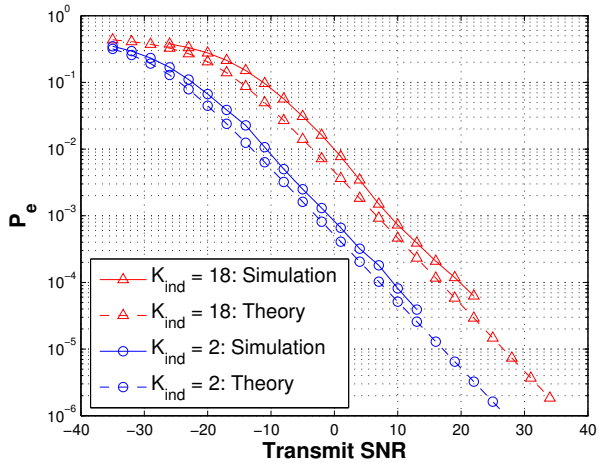

(b)

Fig. 8. (a) P_e vs SNR plots for an AWS system in an ISCM configuration relative to those for high-resolution sensing. (b) Comparison of the analytically computed P_e values with numerically estimated values for the non-ideal scenario.

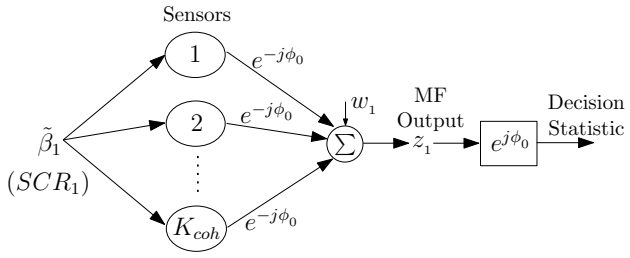

Fig. 9. The K_{coh} sensor transmissions in each SCR are *coherently* mapped to a single MF output at the WIR.

identical transmissions are coherently combined at the receiver after matched filtering to the K-dimensional angle-delay signatures $\boldsymbol{q}_i$, $i = 1, \ldots, K_{ind}$. However, in the process, all K MF outputs, along with their individual noises, contribute to the decoding of the independent bit from each SCR. In the ISCM scenario, we reduce the number of noise sources to K_{ind} by converting the K_{coh} parallel channels between the sensors in each SCR and the WIR into a $K_{coh} \times 1$ MAC (see Fig. 7(c)). However, due to the phase incoherence in the sensors' transmitted signals, we take a significant loss in SNR in long-term P_e performance, due to a form of fading.

Coherent source-channel matching (CSCM) builds on the ISCM configuration with reduced angle-delay resolution, as illustrated in Fig. 9. The motivation for CSCM is to coordinate the phases of the transmissions from the K_{coh} sensors in each SCR so that, in effect, they are *coherently* combined during communication over the channel and the combined signal gets mapped to a single angle-delay bin at the WIR. Thus, CSCM converts the $K_{coh} \times 1$ *incoherent* MAC connecting each SCR to the WIR in the ISCM case to a $K_{coh} \times 1$ *coherent* MAC, as illustrated in Fig. 9. As in ISCM, the first two steps in CSCM involve the reduction in the angular resolution and the delay resolution (refer Figs. 7 (a) and (b)). However, CSCM differs from ISCM in the third crucial step, where the K_{coh} sensors in each group that now lie in a single angle-delay bin in Fig. 7(b) transmit in a *phase-coherent* fashion, as illustrated in Fig. 9. A detailed discussion of techniques to realize CSCM in practice is given in Sec. VI-B.

The effective system equation for CSCM can be expressed using (33) as

$$\boldsymbol{z}_{csc} = \sqrt{M\mathcal{E}}\boldsymbol{Q}^H\boldsymbol{Q}\tilde{\boldsymbol{\beta}} + \boldsymbol{w}_{csc} = \sqrt{M\mathcal{E}}\sum_{i=1}^{K_{ind}} \tilde{\beta}_i \boldsymbol{v}_i + \boldsymbol{w}_{csc} \quad (54)$$

where $\boldsymbol{z}_{csc} = [z_{csc,1}, z_{csc,2}, \ldots, z_{csc,K_{ind}}]^T$ and the $K_{ind} \times K_{ind}$ signature matrix

$$\boldsymbol{V} = \boldsymbol{Q}^H\boldsymbol{Q} = [\boldsymbol{v}_1, \cdots, \boldsymbol{v}_{K_{ind}}] = [\boldsymbol{Q}^H\boldsymbol{q}_1, \cdots, \boldsymbol{Q}^H\boldsymbol{q}_{K_{ind}}] \quad (55)$$

represents the coherent coupling between the K_{ind} independent bits and the K_{ind} active angle-delay bins at the WIR, and the $K_{ind} \times 1$ vectors, $\{\boldsymbol{v}_i\}$, represent the effective *angle-delay focussed* signatures associated with the i-th transmitted bit $\tilde{\beta}_i$. Due to the coherent angle-delay focussing, we have the following relation between $\boldsymbol{v}_i$, $\boldsymbol{q}_i$ and $\boldsymbol{\gamma}_i$

$$\|\boldsymbol{v}_i\|^2 \approx K_{coh}\|\boldsymbol{q}_i\|^2 \approx K_{coh}^2\|\boldsymbol{\gamma}_i\|^2 = K_{coh}^2 \ , \quad (56)$$

where the approximations are exact in the ideal case. Recall that the ISCM signatures are random (due to incoherent sensor transmissions) and satisfy $E[\|\boldsymbol{d}_i\|^2] = \|\boldsymbol{q}_i\|^2 = K_{coh}$.

As in the previous cases, the receivers for CSCM can be designed using the system equation (54). The signature matched filter receiver is given by $\hat{\tilde{\boldsymbol{\beta}}}_{mf} = \text{sign}\left\{\text{Re}\left(\boldsymbol{V}^H\boldsymbol{z}_{csc}\right)\right\}$ and $P_{e,csc,mf}(i) = Q\left(\sqrt{2\text{SINR}_{\text{mf}}(\text{i})}\right)$ can be computed by using the expression for $\text{SINR}_{mf}(i)$ in (38) by replacing $\{\boldsymbol{q}_i\}$ with $\{\boldsymbol{v}_i\}$. Similarly, the MMSE receiver is given by $\hat{\tilde{\boldsymbol{\beta}}}_{mmse} = \text{sign}\left\{\text{Re}\left(\boldsymbol{L}_{csc,mmse}\boldsymbol{z}_{csc}\right)\right\}$ where the $K_{ind} \times K_{ind}$ matrix $\boldsymbol{L}_{csc,mmse}$ is given by

$$\boldsymbol{L}_{csc,mmse} = \boldsymbol{V}^H\boldsymbol{R}_{csc}^{-1} \quad (57)$$

and $\boldsymbol{R}_{csc} = E[\boldsymbol{z}_{csc}\boldsymbol{z}_{csc}^H] = M\mathcal{E}\boldsymbol{V}\boldsymbol{V}^H + \sigma^2\boldsymbol{I}$. The corresponding probability of error, $P_{e,csc,mmse}$, can be computed using (50) by replacing $\{\boldsymbol{d}_i\}$ with $\{\boldsymbol{v}_i\}$ and $\boldsymbol{R}_{isc}$ with $\boldsymbol{R}_{csc}$.

Remark 6 (Ideal Case): When all the sensors in each SCR coincide with the center of the resolution bins at the highest

resolution, $\boldsymbol{\Gamma} = \boldsymbol{\Phi}$ is diagonal (see Rem. 1), $\boldsymbol{Q} = \boldsymbol{\Phi}\boldsymbol{U}$ and from (55) we have $\boldsymbol{V} = \boldsymbol{U}^H\boldsymbol{\Phi}^H\boldsymbol{\Phi}\boldsymbol{U} = K_{coh}\boldsymbol{I}$. In the high resolution case, the $K \times 1$ signature $\boldsymbol{q}_i$ consists of all zeros except K_{coh} unit magnitude (phase) entries in the coordinates corresponding to the i-th SCR. On the other hand, the "focussed" $K_{ind} \times 1$ signature $\boldsymbol{v}_i$ consists of all zeros except a non-zero entry of size K_{coh} in the coordinate corresponding to the i-th SCR. The increase in magnitude of the non-zero entry is due to the phase-coherent transmissions from K_{coh} sensors in the SCR (see Fig. 9). Thus, the signature vectors are orthogonal, $\boldsymbol{V}^H\boldsymbol{V} = K_{coh}^2\boldsymbol{I}$, and the energy coupled to the WIR from each SCR, $\|\boldsymbol{v}_i\|^2 = K_{coh}\|\boldsymbol{q}_i\|^2 = K_{coh}^2$, is a factor of K_{coh} higher than that at the highest resolution. In relation to the ISCM configuration, CSCM corresponds to aligning the phases of sensors in each SCR so that they contribute coherently to the corresponding MF output, resulting in the highest SNR at the receiver. □

The P_e in the ideal case is useful in comparing the performance of the CSCM relative to information retrieval at the highest resolution and ISCM:

$$P_{e,csc,ideal} = Q\left(\frac{\sqrt{2M\mathcal{E}\|\boldsymbol{v}_i\|^2}}{\sigma^2}\right) = Q\left(\sqrt{\frac{2M\mathcal{E}}{\sigma^2}\left(\frac{K}{K_{ind}}\right)^2}\right)$$
$$= Q\left(\sqrt{\frac{2M\mathcal{E}K_{coh}^2}{\sigma^2}}\right) . \tag{58}$$

Comparing the above expression with (40) we note that CSCM affords an SNR gain of K_{coh} compared to information retrieval at the highest resolution and does not suffer the loss in performance due to fading in ISCM (see (53)).

A. Numerical Results

We now present numerical results to illustrate the performance of information retrieval with CSCM. The simulation set up is the same as in Sec. IV-C. The P_e as a function of the per-sensor transmit SNR, ρ_{sen}, is shown in Fig. 10(a). Note that although the P_e behavior as a function of K_{ind} is similar to that of the maximum resolution case, the SNR required to attain a desired P_e is substantially reduced due to the K_{coh} SNR gain. For the matched filter receiver, there is a loss in SNR in the non-ideal case and also a P_e floor due to interference, as expected. However the performance is near-ideal for the MMSE receiver. Note that the phase-coherent sensor transmissions eliminate the detrimental phenomenon of fading which dominated the P_e behavior in the case of ISCM. Coherent source-channel matching effectively corresponds to an ISCM system with the highest instantaneous SINR (coherent sensor phases). Fig. 10(b) compares the performance gains due to coherent SCM relative to information retrieval at the highest resolution. Even in the non-ideal case, CSCM provides an SNR gain of approximately $10\log(K_{coh})$ dB compared to information retrieval at the maximum resolution. For example, when $K_{ind} = 6 \Rightarrow K_{coh} = 18$, the P_e curves are spaced by about 12dB. For a constant K, decreasing K_{ind} increases K_{coh} and hence the gain due to CSCM is even more pronounced for smaller values of K_{ind}.

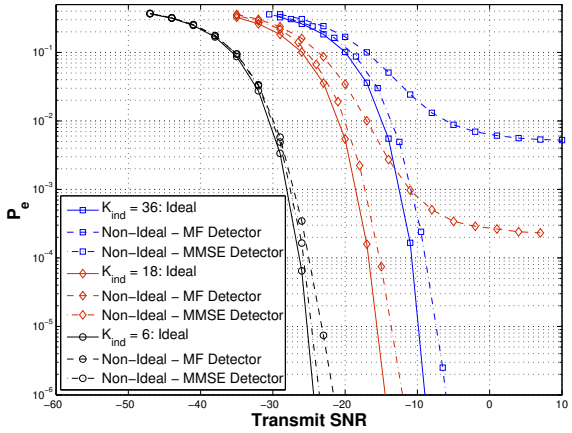

(a)

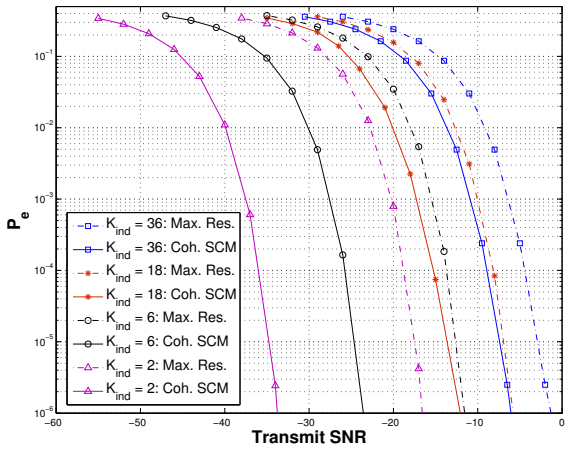

(b)

Fig. 10. (a) P_e vs SNR plots for an AWS system using CSCM with K_{ind} bits retrieved in each channel use. (b) Comparison of AWS performance at the maximum resolution and CSCM. Non-Ideal P_e curves for MMSE detector.

B. Realizing the Source-Channel Matched Architecture

How do we adapt the angle-delay resolution in source-channel matching, illustrated in Figs. 7 and 9? The reduction in angular resolution can be achieved by reducing the antenna spacings at the WIR by a factor of M_{coh} ($M_{coh} = 3$ in Fig. 7) [25], [26]. This effectively results in $M/M_{coh} = M_{ind}$ distinct spatial beams, each with a M_{coh} times wider beamwidth [25], [26]. Alternatively, the carrier frequency could be reduced by a factor M_{coh} to attain the same effect. The delay resolution could be reduced by a factor L_{coh} by decreasing the signaling bandwidth by a factor L_{coh}, as in Fig. 7(b). Alternatively, distributed time-reversal techniques [31] can also be used to line up the sensor transmissions in L_{coh} ($L_{coh} = 4$ in the figure) distinct delay bins into a single delay bin. The above two steps reduce the angle-delay resolution, so that it is matched to the size of the SCRs in the sensing configuration. Finally, distributed beamforming algorithms [32] could be applied in each SCR to make the K_{coh} sensor transmissions from a single angle-delay bin in Fig. 7(b), phase coherent.

VII. Sensing Capacity

Thus far we have analyzed the performance of AWS for *uncoded* coherent BPSK transmissions from the sensors. In this section, we discuss the notion of sensing capacity in AWS – the highest rate of information retrieval – that may be attained via *coded* transmissions from the sensors. Furthermore, we address the following question: how does the sensing capacity vary for different sensing configurations as a function of K_{ind} and the per-sensor transmit SNR (ρ_{sen})? As we will see, the answer in the case of coherent source-channel matching is surprising and reflects the SNR gain proportional to K_{coh}^2.

As mentioned earlier, AWS effectively creates a semi-distributed MIMO channel between the K sensors and the WIR via angle-delay matched filtering. The capacity for any given sensing configuration is governed by the underlying matrix, $\boldsymbol{H}$, that couples the K_{ind} SCRs and the WIR: $\boldsymbol{H} = \boldsymbol{Q}$, $\boldsymbol{D}$, or $\boldsymbol{V}$ in the case of high-resolution sensing, incoherent source-channel matching and coherence source-channel matching, respectively. Using results on the capacity of MIMO channels [33], the sensing capacity of AWS, conditioned on a given realization of $\boldsymbol{H}$, can be computed as

$$\begin{aligned} C\left(K_{ind}\right) &= \frac{1}{TW+L}\log_2\left|\boldsymbol{I}+\frac{\mathcal{E}M}{\sigma^2}\boldsymbol{H}\boldsymbol{H}^H\right| \\ &\approx \frac{1}{TW+L}\sum_{i=1}^{K_{ind}}\log_2\left(1+\mathrm{SINR}(i)\right) \quad \text{b/s/Hz} \end{aligned} \tag{59}$$

where (59) reflects the mutual information of a MIMO channel characterized by $\boldsymbol{H} = \{\boldsymbol{Q}, \boldsymbol{D}, \boldsymbol{V}\}$ under the assumption of equal power and independent transmissions from the different SCRs, and the factor $TW+L$ is the signaling time-bandwidth product for each channel use. The second approximation in (59) reflects the sum capacity of the K_{ind} parallel channels between the sensor ensemble and the WIR and can be used for estimating capacity with the matched filter or the MMSE receiver by plugging in the appropriate expression for $\mathrm{SINR}(i)$.

To study the impact of sensing configuration and coherent source-channel matching, we focus on the ideal case to get insight so that $\mathrm{SINR} \to \mathrm{SNR}$ and it is the same for all parallel channels. As our numerical results indicate, the analysis in the ideal case accurately reflects the capacity in the non-ideal case. Furthermore, the capacity expression in the ideal case is exact and corresponds to the capacity of K_{ind} parallel AWGN channels, each operating at the same SNR. We primarily consider two cases: maximum resolution, $\boldsymbol{H} = \boldsymbol{Q}$, and coherent SCM, $\boldsymbol{H} = \boldsymbol{V}$. In the former case, (59) simplifies to

$$C_{ideal}\left(K_{ind}\right) = \frac{K_{ind}}{TW+L}\log_2\left(1+\frac{M\mathcal{E}}{\sigma^2}\frac{K}{K_{ind}}\right) \tag{60}$$

whereas in the case of coherent SCM we have

$$C_{ideal,csc}\left(K_{ind}\right) = \frac{K_{ind}}{TW+L}\log_2\left(1+\frac{M\mathcal{E}}{\sigma^2}\left(\frac{K}{K_{ind}}\right)^2\right) \tag{61}$$

which reflects an SNR gain of K_{coh} per parallel channel compared to the maximum resolution case.

From (60) we note that the sensing capacity is a monotonic function of K_{ind} in the maximum resolution case. This is illustrated in Fig. 11(a) where the capacity for the non-ideal case with the MMSE receiver (using the approximation in (59)) is plotted as a function of per-sensor transmit SNR, ρ_{sen}. As evident, at high SNRs, the capacity is maximum for $K_{ind} = K$ and minimum for $K_{ind} = 1$. On the other hand, this increase in capacity with K_{ind} diminishes at low SNRs and the two curves coincide.

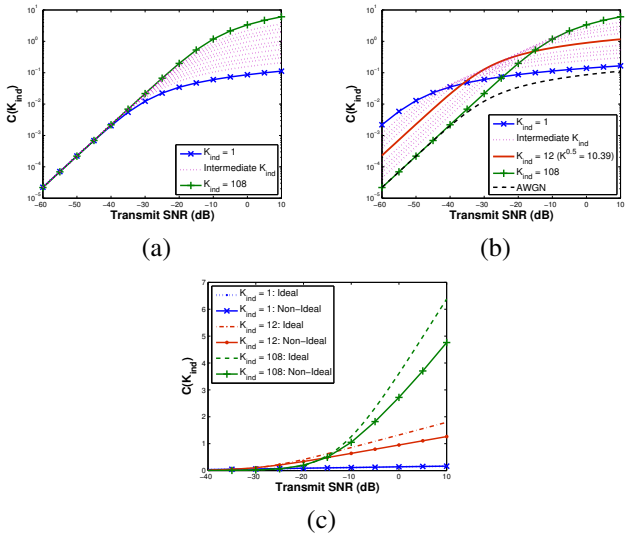

Fig. 11. Sensing capacity of AWS with the MMSE receiver (non-ideal case) as a function of ρ_{sen} for different values of K_{ind}. (a) Information retrieval at maximum resolution. (b) Information retrieval with coherent source-channel matching (c) Comparison of the capacity, plotted on a linear scale, in the ideal case with that in the non-ideal case with CSCM.

Fig. 11(b) plots the non-ideal sensing capacity as a function of ρ_{sen} for coherent SCM for different values of K_{ind}. In this case, the capacity is not a monotonic function of ρ_{sen}. At high SNRs, the $K_{ind} = K$ configuration yields the highest capacity, as in the high resolution case, whereas $K_{ind} = 1$ yields the lowest capacity. However, at low SNRs, the roles are reversed: the $K_{ind} = 1$ configuration yields the highest capacity and $K_{ind} = K$ yields the lowest capacity. Most importantly, at every ρ_{sen} there is an optimum sensing configuration, $K_{ind,opt}(\rho_{sen})$, that yields the highest capacity. In particular, the configuration $K_{ind} = \sqrt{K}$ is a robust choice whose capacity remains between the extreme cases of $K_{ind} = K$ and $K_{ind} = 1$. In fact, the expression for $C_{csc,ideal}$ reveals a fundamental *multiplexing gain versus received SNR tradeoff* that we have also recently discovered in the context of MIMO communication over sparse multipath channels [25], [26]: increasing the multiplexing gain (K_{ind}) comes at the cost of decreasing the received SNR per parallel channel, $\rho_{rx} = \rho_{sen}M(K/K_{ind})^2$, and vice versa. The optimal configuration at any ρ_{sen} optimizes this tradeoff to yield the highest capacity. Using the results of [25], [26], we can characterize the optimal configuration in the ideal case, for any operating ρ_{sen}, as

$$K_{ind,opt,csc}(\rho_{sen}) \approx \begin{cases} 1 & , \quad \rho_{sen} \le \rho_{low} = \frac{4}{MK^2} \\ \frac{\sqrt{M\rho_{sen}}K}{2} & , \quad \rho_{sen} \in (\rho_{low}, \rho_{high}) \\ K & , \quad \rho_{sen} \ge \rho_{high} = \frac{4}{M} \end{cases} \tag{62}$$

Fig. 11(b) also shows the capacity of an equivalent AWGN

channel with the total receive SNR $\rho_{total} = \rho_{sen}MK$ reflecting the situation in which a single sensor (a fusion node) transmits the data using the total power used by the entire ensemble of K nodes. As evident, optimized coherent SCM affords the maximum multiplexing gain over the AWGN capacity over the entire SNR range, reflecting the K-fold distributed MIMO capacity gain. Fig. 11(c) compares the capacity in the ideal and non-ideal cases for CSCM on a linear scale to emphasize any loss due to interference. The deviation between ideal and non-ideal cases is relatively small and increases with larger K_{ind} due to higher interference.

VIII. In-network Processing versus AWS: Energy and Latency

In this section, we compare in-network processing and AWS in terms of *energy* and *latency* requirements for achieving *consensus* in a sensor network – a canonical example of in-network processing that involves computation of the *average* of all sensor measurements and making it available at each node in the network. In particular, we compare iterative gossip algorithms [4], [5], [7], that achieve consensus using multi-hop communications, with achieving consensus in AWS using the canonical sensing model in Sec. III. We show that for a sufficiently large network, AWS achieves consensus with lower energy and latency compared to gossip algorithms, and the performance gap increases with the network size.

Recall from Sec. III that the sensor network is partitioned as $K = K_{ind}K_{coh}$ into K_{ind} SCRs, each with K_{coh} nodes. The sensors in each SCR have identical measurements, whereas the measurements in different SCRs are independent. Let $\mathcal{E}_{rx}$ be the received energy (or SNR) required at a sensor or at the WIR for a desired probability of error. The required transmit energy at each sensor node is given by

$$\begin{aligned} &\text{inter-sensor (gossip): } \mathcal{E}_{rx} = \frac{\mathcal{E}_g}{r^\alpha} \\ &\text{sensor-WIR (AWS): } \mathcal{E}_{rx} = \frac{\mathcal{E}_{aws}}{R^\alpha} K_{coh}^\mu \end{aligned} \tag{63}$$

where $\alpha \geq 2$ denotes the path loss coefficient, and r and R denote the average inter-sensor distance and the average distance between the sensor ensemble and the WIR, respectively. The parameter $\mu \in \{1, 2\}$ reflects the SNR gain in AWS: $\mu = 1$ corresponds to high-resolution sensing with an SNR gain of K_{coh}, and $\mu = 2$ corresponds to coherent SCM with an SNR gain of K_{coh}^2 (see Secs. IV and VI). Equating $\mathcal{E}_{rx}$ in the two cases yields the following relation

$$\frac{\mathcal{E}_{aws}}{\mathcal{E}_g} = \frac{1}{K_{coh}^\mu} \left(\frac{R}{r}\right)^\alpha \tag{64}$$

between the required (per-sensor) transmit energy in AWS ($\mathcal{E}_{aws}$) and in-network gossip algorithms ($\mathcal{E}_g$).

Standard gossip algorithms require $\mathcal{O}(K^2)$ sensor transmissions (and channel uses) to achieve consensus [5], and hence both the *latency*, D_g, and the *total energy*, $\mathcal{E}_{tot,g}$ grow at this rate.[5] In AWS, on the other hand, consensus can be achieved in just two channel uses: the K sensors transmit their measurements to the WIR (one channel use), and the WIR then computes the average and broadcasts it simultaneously (one channel use) to the entire ensemble. Hence, the latency in AWS, D_{aws}, is $\mathcal{O}(1)$ and total number of sensor transmissions, and hence the total energy, $\mathcal{E}_{tot,aws}$, scales as $\mathcal{O}(K)$. These trends do not change even if we include training and phase estimation, since they also require $O(1)$ channel uses. Thus, we arrive at the following energy and latency relations between AWS and gossip algorithms

$$\begin{aligned} &\text{energy}: \frac{\mathcal{E}_{tot,aws}}{\mathcal{E}_{tot,g}} \propto \frac{K\mathcal{E}_{aws}}{K^2\mathcal{E}_g} = \frac{1}{KK_{coh}^\mu}\left(\frac{R}{r}\right)^\alpha \propto \frac{1}{K^{\mu+1}}\left(\frac{R}{r}\right)^\alpha \\ &\text{latency}: \frac{D_{aws}}{D_g} \propto \frac{1}{K^2} \end{aligned} \tag{65}$$

where we have used (64) and the fact that $K_{coh} \sim \mathcal{O}(K)$ in the energy relations.

As evident, AWS has a definitive and very significant latency advantage due to the iterative nature of in-network processing algorithms and a convergence rate that is generally *super-linear* in the number of nodes. This also confers an energy advantage to AWS (the $1/K^{\mu+1}$ factor in the energy relation), but this advantage is offset by the higher energy required in AWS due to single-hop transmissions over a longer distance (the $(R/r)^\alpha$ factor in the energy relation). For a given K, R, r and α, we arrive at the following conditions for AWS being more energy efficient if

$$K > \left(\frac{R}{r}\right)^{\frac{\alpha}{\mu+1}} \Leftrightarrow \left(\frac{R}{r}\right) < K^{\frac{\mu+1}{\alpha}} \ . \tag{66}$$

Thus, AWS is more energy efficient if the number of nodes K is sufficiently large for a given R/r, or if the distance ratio R/r is sufficiently small for a given K. Furthermore, these trends hold even without coherent source-channel matching ($\mu = 1$) in AWS, and the energy advantage of AWS becomes more pronounced with increasing K for a fixed (R/r).

Some remarks about the above comparison are in order. First, we have ignored the additional coordination and routing costs in in-network processing. Furthermore, such iterative algorithms require that the inter-sensor distance r increases with K to control inter-sensor interference (e.g., r is required to grow as $\sqrt{K/\log(K)}$ in [5]). In practice, both these factors will result in increased energy consumption with K. Second, while coherent SCM ($\mu = 2$) is more energy efficient than high resolution sensing ($\mu = 1$) in AWS, we have not accounted for the cost in achieving phase-synchronized sensor transmissions in each SCR. The energy and delay requirements of state-of-the-art distributed phase synchronization algorithms grow linearly with $K_{coh} \sim \mathcal{O}(K)$ [32], thereby limiting the advantage of coherent SCM if phase synchronization is needed often. On the other hand, AWS affords an M-fold array gain in energy consumption, which we have not accounted for – larger array sizes become feasible at higher carrier frequencies. Finally, the above comparison is based on the canonical sensor correlation model in AWS which assumes that sensors in a given SCR have *identical* measurements. In practice, this would not be the case. One natural approach for achieving this in practice

[5] If the sensors know their relative locations, *geographic* gossip algorithms can be used that require $\mathcal{O}(K^{3/2}\sqrt{\log(K)})$ channel uses [5], which is still *super-linear* in K.

is to combine AWS and in-network processing: use gossip-type algorithms within each SCR to achieve local consensus, and then use AWS to achieve global consensus. In this case, the total energy consumed will have two components: one due to in-network processing within each SCR which will grow as $\mathcal{O}(K_{coh}^2)$, and one due to out-of-network communication via AWS which will grow as $\mathcal{O}\left(\frac{K}{K_{coh}^{\mu}}(R/r)^{\alpha}\right)$. Thus, an optimum size of SCRs, K_{coh}, could be determined to minimize the overall energy consumption by balancing the two terms.

IX. Conclusions

Active Wireless Sensing (AWS) provides an alternative to in-network processing in sensor networks and exploits the advanced functionality afforded by emerging wideband, agile RF front-ends and reconfigurable antenna arrays for rapid and energy-efficient information retrieval. It also serves as a basic building block for facilitating network communication, monitoring and control in mesh topologies. The key underlying idea in AWS is to distinguish individual sensor responses by exploiting the differences in the space-time (angle-delay) signatures generated by them. Our analysis based on the canonical sensing configurations and source-channel matching shows that adapting the spatio-temporal resolution in AWS to the spatial correlation in the signal field (or the spatial scale of cooperation in the network) can greatly enhance energy efficiency. In particular, coherence source-channel matching yields the highest gains in terms of energy efficiency and rate of information retrieval. In comparison to in-network processing, AWS has a definite and significant latency advantage that grows with the size of the network. Furthermore, for a given distance between the WIR and the sensor ensemble, our preliminary energy analysis suggests that AWS is more energy efficient for a sufficiently large number of sensor nodes.

There are many exciting avenues for future work. First, while the focus of this paper was on line-of-sight (LOS) communication, in practice the sensing channel will likely involve multipath scattering between the sensor ensemble and the WIR. Our initial results in this challenging scenario indicate that multipath, in addition to LOS, can further enhance energy efficiency [34]. On the other hand, sensor localization information that is readily available in the LOS scenario is compromised. However, time-reversal techniques could be leveraged for sensor localization in the presence of multipath [35]. Second, while we assumed perfect knowledge of the signature matrices $(\boldsymbol{\Gamma}, \boldsymbol{Q}, \boldsymbol{D}, \boldsymbol{V})$ in this paper, they will need to be estimated in practice. Thus, analysis of the impact of estimation errors on the performance of AWS would be useful for practical implementation. In this regard, developing non-coherent communication protocols in AWS is also an interesting direction. Finally, extending recent work on data-driven modulation (see, e.g., [15], [16], [36], [37]) in the context of AWS would also be fruitful.

References

[1] D. Estrin, L. Girod, G. Pottie, and M. Srivastava, "Instrumenting the world with wireless sensor networks," in *Proc. IEEE Intl. Conf. on Acoustics, Speech, and Signal Processing (ICASSP'01)*, vol. 4, May 2001, pp. 2033–2036.

[2] I. Akyildiz, W. Su, Y. Sankarasubramaniam, and E. Cayirci, "A survey on sensor networks," *IEEE Communications Magazine*, vol. 40, no. 8, pp. 102–114, Aug. 2002.

[3] *IEEE Journal on Selected Areas in Communications*. Special Issues on Sensor Networks, Aug. 2004 and Apr. 2005.

[4] J. Chen, G. Pandurangan, and D. Xu, "Robust computation of aggregates in wireless sensor networks: Distributed randomized algorithms and analysis," in *Proc. 4th Intl. Conf. on Information Processing in Sensor Networks (IPSN'05)*, Apr. 2005, pp. 348–355.

[5] A. G. Dimakis, A. D. Sarwate, and M. Wainwright, "Geographic gossip : Efficient aggregation for sensor networks," in *Proc. 5th Intl. Conf. on Information Processing in Sensor Networks (IPSN'06)*, Nashville, TN, Apr. 2006, pp. 69–76.

[6] A. Giridhar and P. Kumar, "Computing and communicating functions over sensor networks," *IEEE Journal on Selected Areas in Communications*, vol. 23, no. 4, pp. 755–764, Apr. 2005.

[7] S. Boyd, A. Ghosh, B. Prabhakar, and D. Shah, "Randomized gossip algorithms," *IEEE Transactions on Information Theory*, vol. 52, no. 6, pp. 2508–2530, June 2006.

[8] P. Gupta and P. Kumar, "Towards an information theory of large networks: An achievable rate region," *IEEE Transactions on Information Theory*, vol. 49, no. 8, pp. 1877–1894, Aug. 2003.

[9] *Center for Embedded Networked Sensing*. http://www.cens.ucla.edu.

[10] T. Sivanadyan and A. Sayeed, "Active wireless sensing for rapid information retrieval in sensor networks," in *Proc. 5th Intl. Conf. on Information Processing in Sensor Networks (IPSN'06)*, Apr. 2006, pp. 85–92.

[11] A. Sayeed and T. Sivanadyan, "Source channel communication protocols and tradeoffs in active wireless sensing," in *Proc. 44th Annual Allerton Conference on Communication, Control and Computing*, Sep. 2006.

[12] R. Nowak, U. Mitra, and R. Willett, "Estimating inhomogeneous fields using wireless sensor networks," *IEEE Journal on Selected Areas in Communications*, vol. 22, no. 6, pp. 999–1006, Aug. 2004.

[13] M. Gastpar and M. Vetterli, "Power, spatio-temporal bandwidth, and distortion in large sensor networks," *IEEE Journal on Selected Areas in Communications*, vol. 23, no. 4, pp. 745–754, Apr. 2005.

[14] A. D'Costa, V. Ramachandran, and A. M. Sayeed, "Distributed classification of gaussian space-time sources in wireless sensor networks," *IEEE Journal on Selected Areas in Communications*, vol. 22, no. 6, pp. 1026–1036, Aug 2004.

[15] G. Mergen and L. Tong, "Type based estimation over multiaccess channels," *IEEE Transactions on Signal Processing*, vol. 54, no. 2, pp. 613–626, Feb. 2006.

[16] K. Liu and A. Sayeed, "Type-based decentralized detection in wireless sensor networks," *IEEE Transactions on Signal Processing*, vol. 55, no. 5, pp. 1899–1910, May 2007.

[17] W. U. Bajwa, A. M. Sayeed, and R. Nowak, "Matched source-channel communication for field estimation in wireless sensor networks," in *Proc. 4th Intl. Conf. on Information Processing in Sensor Networks (IPSN '05)*, Apr. 2005, pp. 332–339.

[18] *IEEE J. Select. Areas Commun.* Special issue on Adaptive, Spectrum Agile and Cognitive Wireless Networks, April 2007.

[19] S. Haykin, "Cognitive radio: Brain-empowered wireless communications," *IEEE Journal on Selected Areas in Communications*, vol. 23, no. 2, pp. 201–220, Feb 2005.

[20] *IEEE Journal on Selected Topics in Signal Processing*. Special Issue on Adaptive Waveform Design for Agile Sensing and Communication, June 2007.

[21] B. Ananthasubramaniam and U. Madhow, "Virtual radar imaging for sensor networks," in *Proc. 3rd Intl. Conf. on Information Processing in Sensor Networks (IPSN'04)*, Apr. 2004, pp. 294–300.

[22] ——, "Detection and localization of events in imaging sensor nets," in *Proc. IEEE Intl. Symp. on Information Theory (ISIT'05)*, Sep. 2005, pp. 825–829.

[23] A. Sayeed, "Deconstructing multi-antenna fading channels," *IEEE Transactions on Signal Processing*, vol. 50, no. 10, pp. 2563–2579, Oct. 2002.

[24] ——, "A virtual representation for time- and frequency-selective correlated mimo channels," in *Proc. IEEE Intl. Conf. on Acoustics, Speech, and Signal Processing (ICASSP'03)*, vol. 4, May 2003, pp. 648–651.

[25] A. Sayeed and V. Raghavan, "The ideal MIMO channel: Maximizing capacity in sparse multipath with reconfigurable antenna arrays," in *Proc. IEEE Intl. Symp. on Information Theory*, July 2006, pp. 1033–1040.

[26] ——, "Maximizing MIMO capacity in sparse multipath with reconfigurable antenna arrays," *IEEE Journal of Selected Topics in Signal Processing*, vol. 1, no. 1, pp. 156–166, June 2007.

[27] J. G. Proakis, *Digital Communications*, 4th ed. McGraw-Hill, 2001.

[28] S. Verdu, *Multiuser Detection*. Cambridge University Press, 1998.
[29] S. Haykin, *Adaptive Filter Theory*, 4th ed. Prentice Hall, 2002.
[30] T. Kadous and A. Sayeed, "Decentralized multiuser detection for time-varying multipath channels," *IEEE Transactions on Communications*, vol. 48, no. 11, pp. 1840–1852, Nov. 2000.
[31] R. J. Barton, J. Chen, and K. Huang, "Cooperative time reversal for communication in power-constrained wireless sensor networks," in *Proc. 43rd Annual Allerton Conference on Communication, Control and Computing*, Sep. 2005.
[32] R. Mudumbai, J. Hespanha, and U. Madhow, "Scalable feedback control for distributed beamforming in sensor networks," in *Proc. IEEE Intl. Symp. on Information Theory (ISIT'05)*, Sep. 2005, pp. 137–141.
[33] E. Telatar, "Capacity of multi-antenna Gaussian channels," *AT& T-Bell Labs Internal Tech. Memo.*, June 1995.
[34] T. Sivanadyan and A. Sayeed, "Active wireless sensing in multipath environments," in *IEEE Statistical Signal Processing Workshop*, Madison, WI, Aug. 2007, pp. 378–382.
[35] ——, "Space-time reversal techniques for information retreival in wireless sensor networks," in *Sensor, Signal and Information Processing Workshop (SenSIP'08)*, Sedona, AZ, May 2008.
[36] Y. Hong and A. Scaglione, "Distributed change detection in large scale sensor networks through the synchronization of pulse-coupled oscillators," in *Proc. IEEE Intl. Conf. on Acoustics, Speech and Signal Processing (ICASSP'04)*, May 2004.
[37] K. Liu, H. El Gamal, and A. Sayeed, "Decentralized inference over multiple access channels," *IEEE Transactions on Signal Processing*, vol. 55, no. 7, pp. 3445–3455, July 2007.